

## Research paper

## A mission concept for removing multiple debris using formation-flying slingshot spacecraft

Achira Boonrath<sup>a</sup>, Federico Rossi<sup>b</sup>, Issa A. Nesnas<sup>b</sup>, Eleonora M. Botta<sup>a</sup>,\*<sup>a</sup> Department of Mechanical and Aerospace Engineering, University at Buffalo, Buffalo, NY, United States<sup>b</sup> Jet Propulsion Laboratory, California Institute of Technology, La Cañada Flintridge, CA, United States

## ARTICLE INFO

## Keywords:

Active debris removal  
Robotic net system  
Deorbiting  
Rendezvous and proximity operations  
Space mission design

## ABSTRACT

To mitigate the threat posed by the increasing quantity of space debris populating Low Earth Orbit, innovative, efficient, and cost-effective solutions must be developed to perform active debris removal. To address this need, the REusable Spacecraft Teams for on-Orbit debris REmoval (RESTORE) concept is proposed, comprising a team of three or more spacecraft carrying a net that captures and deorbits small-sized debris through dragging and *slingshot ejection* maneuvers. A preliminary design analysis of the system is performed in this work to demonstrate the feasibility of the concept. The system performance throughout the different phases of the debris removal mission is evaluated by examining the results of dynamics simulations. Multiple debris removal mission architectures are examined along with systems engineering of the spacecraft. The RESTORE system is shown to efficiently remove small- to medium-sized debris with sufficient safety and delta-v margins.

## 1. Introduction

Low Earth Orbit (LEO) is home to satellites performing many crucial missions, including providing communication services (e.g., SpaceX's Starlink), weather forecasting, and Earth environmental monitoring. However, these satellites are threatened by the increasing amounts of space debris populating LEO; as indicated in Ref. [1], over 3000 tons of space debris occupy the region. The collision of debris with other debris or with an active satellite (as in the Cosmos 2201 and Iridium 33 collision [2]) has a cascading effect that grows debris fragments. With this threat in mind, innovative, efficient, and cost-effective solutions must be developed to perform active debris removal (ADR).

Proposed ADR methods are classed into contactless and contact-based techniques [3,4]. Contactless methods employ laser-based systems (in space or ground-based) or ion-beam shepherd satellites to impart small forces (and therefore small change in the orbital velocity) on the debris over time. While contactless methods allow the removal systems to be placed at safe distances away from the target, they require precise beam pointing accuracy, very long deorbiting mission time, and have prohibitive upfront development costs [3,4]. In comparison, contact-based ADR techniques offer faster solutions, lower research and development costs, and an overall higher technological readiness level (TRL) in exchange for the need to conduct precise rendezvous and proximity operations. Contact-based methods involve rendezvousing controlled spacecraft with the debris, capturing the latter, and then

deorbiting it or relocating it to unpopulated graveyard orbits [3]. Examples of contact-based ADR concepts include robotic arms and tethered systems [3,4]. Robotic arms consist of links connected through multiple motorized joints with an end-effector mounted, allowing for a high degree of control over the motion of the debris after it has been captured. However, robotic arms require the chaser satellite to match the rotational motion of (potentially uncooperative) debris before grasping, and need features on the target that can be grasped. Tethered ADR concepts involve using one or more flexible cables – reeled from a winch located on a chaser spacecraft – that connect to a debris capture system (e.g., small robots, harpoons, or nets). Among the proposed tethered technologies, tether-nets are considered to be the most promising due to their ability to capture and secure tumbling debris robustly [5–8]. However, most designs for tether-nets do not allow their flight paths to be corrected mid-deployment, and nets can generally be deployed out of the chaser spacecraft once only – i.e., they are not reusable.

The Space Net Robot (SNR) concept – first formulated by Huang et al. [9] – was proposed to further increase the capabilities and robustness to uncertainties of net-based ADR systems. The concept involves using multiple small spacecrafts connected to a net for the capture of space debris, guided via control algorithms for maneuvering right before and during debris capture. Zhu et al. [10,11] studied the capture

\* Corresponding author.

E-mail addresses: [achirabo@buffalo.edu](mailto:achirabo@buffalo.edu) (A. Boonrath), [federico.rossi@jpl.nasa.gov](mailto:federico.rossi@jpl.nasa.gov) (F. Rossi), [issa.a.nesnas@jpl.nasa.gov](mailto:issa.a.nesnas@jpl.nasa.gov) (I.A. Nesnas), [ebotta@buffalo.edu](mailto:ebotta@buffalo.edu) (E.M. Botta).

dynamics of SNRs with debris and the feedback control required to capture multiple debris scattered in very close proximity to each other. Huang et al. [12–15] examined the use of robust control laws to manipulate the configuration of SNRs throughout capture missions. Boonrath et al. and Liu et al. [16,17] explored the use of reinforcement learning for the deployment control of SNRs under the presence of environmental uncertainties. However, existing studies have not considered the required mission profile for the ADR systems to travel to and capture debris located in different orbits, nor the deorbiting phase of the mission and systems engineering aspects.

Similar to the SNR concept, but independently conceived, this work proposes REusable Spacecraft Teams for on-Orbit debris REmoval (RESTORE) for ADR missions in LEO. The RESTORE system consists of a team of three or more spacecraft carrying a net that captures, traps, and deorbits debris through dragging and novel *slingshot ejection* maneuvers. The slingshot ejection maneuvers consist of the rapid expansion of the net from a compacted form to an almost entirely stretched-out configuration as the debris is enveloped by it. The maneuver imparts a  $\Delta V$  to the debris relative to the capturing spacecraft, altering its speed and path. The RESTORE concept combines the advantage of using traditional net-based techniques – e.g., robustness to uncertainty regarding the system-debris relative position and rotational states – with the reusability of robotic arms.

Unlike previous SNR systems, designed to capture a single debris or multiple debris located in very close proximity to each other (i.e., distances of  $\sim 100$  m apart), the RESTORE system is envisioned to be capable of capturing and deorbiting multiple debris that are located on different orbits (i.e., distances of  $\sim 10$  km apart). For each debris, the removal process has the following phases:

- I. Close Rendezvous and Final Approach;
- II. Envelopment;
- III. Dragging;
- IV. Ejection; and
- V. Relocation and Phasing.

This work presents models and analyses for the debris capture and deorbiting phases (e.g., Phases II, III, and IV), as well as for the mission segments where the RESTORE system travels between the targeted debris (e.g., Phases I and V). The study of Phase I considers the entire rendezvous maneuver, in contrast with prior research that traditionally only examines the guidance, control, and dynamics for its terminal portion (i.e., from distances lower than 100 m [9–17]); a novel minimum-energy path-tracking proportional-derivative (PD) control framework is also formulated for the RESTORE system in this Phase. By examining the simulation results presented for the novel ejection maneuver (i.e., Phase IV), preferred design parameters and initial conditions are identified, and insights are acquired regarding the dynamical effects of approximating the system's threads as rigid, massless rods. Using the developed models and the favorable parameters found, multiple ADR mission profiles are proposed and analyzed, considering debris of varying masses and possessing differing orbital altitudes and true anomaly offsets from one another. For the first time, to the authors' knowledge, the subsystem components the RESTORE system is expected to use are identified and selected, and the mass budget for each subsystem is formulated. Overall, the results of this work demonstrate that it is feasible for the RESTORE system to remove multiple small-to-medium-sized debris that are located on different orbits, requiring a propellant amount that is physically practical for the spacecraft to carry; such a finding is the first of its kind for a net-based ADR system.

The rest of this paper is laid out as follows: in Section 2, the RESTORE debris removal mission concept and system are presented. Section 3 details the mathematical models used to represent the system in the different phases of the mission, and the dynamics of critical phases are analyzed in Section 4. Using the defined models and the

insights acquired from the numerical analyses, Section 5 presents multiple candidate debris removal mission designs, extending the previous analyses performed for SNRs, which only considered mission phases right before and after debris capture. Section 6 discusses the systems engineering of the spacecraft. Finally, the findings of this work are summarized in Section 7.

## 2. Concept overview

### 2.1. Selection of debris objects for removal

The goal of RESTORE's ADR mission is to deorbit multiple small-medium-sized debris objects (defined as approximately 0.1–0.5 m in size) located in debris-rich regions within LEO. We target small-medium-sized debris objects because they are difficult for ground-based sensors to track long-term compared to massive debris (such as defunct satellites and rocket upper stages), while still being large enough to incapacitate active spacecraft if accidental collisions occur [1]. In particular, debris in near-circular Sun-Synchronous orbits—located between approximately 770 km and 830 km altitude at approximately 98° inclination—are of interest, as this region has one of the highest debris concentrations [18,19]. To identify specific examples of debris to be removed and locate these, publicly available databases (i.e., Celestrak.org and Space-Track.org [20,21]) can be used.

It should be noted that the identification, and subsequent rendezvous by a controlled chaser spacecraft, of an uncooperative debris was recently demonstrated by the ADRAS-J mission [22]. Although the debris of interest in the ADRAS-J mission is a large (approximately 10 m long) rocket upper stage – and therefore easier to track than the considered debris objects of this work – the mission illustrates the feasibility of performing the necessary tasks required before the capture phase of ADR missions. It is expected that the combined use of ground-based LEO observation systems (e.g., the Space Surveillance Network's GEODSS system [23]) with sensing equipments (e.g., optical sensors) on-board the RESTORE spacecraft will enable identification, short-term tracking, and rendezvous to be performed for a small-medium size debris as well.

### 2.2. Concept of operations

In this study, it is assumed that the launch vehicle can insert the RESTORE system at a location near the orbital position of the first targeted debris, and with similar orbital parameters. At the location of insertion, the RESTORE system is deployed and unfolded (from a compacted configuration) from the launch vehicle. Then, a check of each subsystem (i.e., power, propulsion, attitude determination and control system (ADCS), communication, sensing, and localization) is performed, as well as ensuring that the system is stretched-out to the desired amount. Subsequently, the ADR mission begins with the RESTORE system performing close-range rendezvous and final approach maneuvers to initiate the capture of the debris. In Phase II, the RESTORE system traps the debris using the net located in the center of the satellite formation. In Phase III, RESTORE applies thrust in the direction opposite to the debris's orbital velocity to reduce the perigee of the coupled system. In Phase IV, it performs the ejection maneuver to rapidly release the debris in the direction opposite to the orbital velocity, thereby slowing it down for direct deorbiting or substantial decrease in orbital lifetime. In this work, the perigee altitude of each debris,  $h_{\text{deo}}$ , is reduced to below approximately 300 km, thereby decreasing the orbital lifetime of debris from the order of decades to the order of months due to the sufficiently high aerodynamic drag [24,25]. At last, the RESTORE system modifies its orbit to travel to the location of the next target in Phase V. The ADR process is repeated until the fuel supply is nearly empty. At that point, the RESTORE system either deorbits itself, or is refueled by a dedicated spacecraft (a possibility that will be explored in future research). Fig. 1 provides visualizations of Phases I–IV of the mission, where the orange arrow indicates the system's direction of travel.

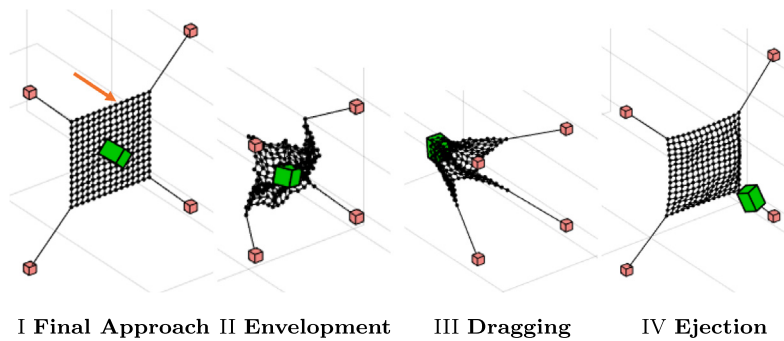


**Fig. 1.** Phases I–IV of debris removal process. (For interpretation of the references to color in this figure legend, the reader is referred to the web version of this article.)

### 2.3. RESTORE system design

The RESTORE system consists of a central net (called the *net proper*) used to wrap and secure debris objects for removal, and robotic corner elements – called Maneuverable Units (MUs) – which are attached to the corners of the net proper via *corner threads*. For this preliminary study, a square net with four MUs attached to its corners was chosen, similar to prior work [6,16,26]; however, we note that other designs – including pyramidal, hexagonal, hemispherical, and conical shapes [8, 27–31] – were also considered by other researchers for net-based ADR systems in general. The net threads are constructed out of high-strength fibers, such as Kevlar or Technora [32]. The MUs are used to maneuver the net to capture debris objects and perform the subsequent deorbiting maneuvers. For a proof-of-concept mission presented in this work, the MUs are conceived as nanosatellites (e.g., 2U–3U CubeSats), but the system could be scaled-up for larger debris. Each MU has subsystems required for autonomous operations in orbit, including sensing and localization, communication, command and control, propulsion, and ADCS. A more detailed consideration of each MU's systems engineering is presented in Section 6.

### 3. Assumptions and dynamical models for the study of the debris removal mission

This Section details the models – and the associated assumptions – employed to perform the preliminary analysis of the multiple debris deorbiting mission. Because of the high concentration of debris in circular orbits around 98° inclination, for this analysis, debris is assumed to be in circular orbits on the same orbital plane. Consequently, all maneuvers are also assumed to happen in the same plane. The initial mass of the RESTORE system is defined as  $m_{\text{sys},0} = 4m_{\text{MU},0} + m_{\text{net}}$ , where  $m_{\text{net}}$  is the mass of the net proper and  $m_{\text{MU},0}$  is the initial (wet) mass of a MU. The RESTORE system is equipped with hydrazine monopropellant engines that are assumed to be perfectly capable of applying thrust as commanded for the MUs; this type of chemical rocket propulsion is chosen since the technology has flight heritage from previous space missions employing small-sized satellites [33]. It is assumed that the thrust control units have perfect knowledge of the system's dynamical states (for the application of feedback control methods), as the development of a state estimation framework is outside of the scope of this work (though it was shown to be possible for a similar, albeit much larger, tethered satellite system in [34,35]). In this work, the attitude motion of the MUs are not considered, since it is assumed that each MU has adequate ADCS capability to properly orient the spacecraft throughout the mission (e.g., through the use of a sliding-model control law alike to that employed for a tethered satellite system in Ref. [35]). Finally, while we acknowledge that accounting for the randomness that could be present within the operational environment is vital for

the overall mission success,<sup>1</sup> comprehensive treatment of the expected uncertainties is outside of the scope of this work. The RESTORE system is expected to be successful in its missions even with environmental uncertainties, based on the fact that previous studies on both passive tether-nets systems and active SNRs (i.e., systems partially similar in function to RESTORE) have demonstrated that they could successfully perform the deployment and debris capture tasks even when mission conditions are not ideal [5,16,36–40].

#### 3.1. Phase I: Close rendezvous and final approach

Phase I of the ADR mission is separated into two stages as follows. First, at the beginning of the *Close Rendezvous* maneuver, the RESTORE system is placed 3000 m behind the debris in the along-track direction, similarly to what was proposed for a debris removal mission in Ref. [41]. Throughout the Close Rendezvous maneuver, the spacecraft moves from 3000 m to a holding position – e.g., 300 m behind the target – on the along-track direction. At the holding position, the spacecraft is stationary relative to the debris to perform its inspection and prepare to conduct the subsequent *Final Approach* maneuver. In the Final Approach maneuver, the spacecraft maneuvers from its holding position to initiate the capture of the debris.

For both stages of Phase I, the Clohessy–Wiltshire–Hill (CWH) equations are used to describe the dynamics of the RESTORE system with respect to the debris. In general, the CWH equations describe the motion of a spacecraft relative to a reference object (in this case, debris) in a circular orbit around the main attracting body (i.e., the Earth) [42]. Each  $i$ th debris possesses a mean motion of  $n_{D,i} = \sqrt{\mu/R_i^3}$ , where  $R_i$  is the orbit radius and  $\mu = 3.986 \times 10^5 \text{ km}^3/\text{s}^2$  is the Earth's standard gravitational parameter. To use the CWH equations, the local vertical, local horizontal (LVLH) frame  $D = \{D, \hat{i}, \hat{j}, \hat{k}\}$  is defined with its origin centered and fixed to (i.e., such that it orbits along with) the center of mass (CoM) of the debris  $D$ . The directions  $\{\hat{i}, \hat{j}, \hat{k}\}$  of the  $D$  frame represent the radial, along-track, and cross-track directions of the orbit, respectively. It should be noted that, since each  $i$ th debris is assumed to be in a circular orbit, the  $\hat{i}$ ,  $\hat{j}$ , and  $\hat{k}$  directions are aligned with the orbital position, velocity, and angular momentum of the debris, respectively. The LVLH frame is drawn in Fig. 2, with the Earth-centered inertial frame  $O = \{O, \hat{i}, \hat{j}, \hat{k}\}$  (about which the debris orbits), the debris orbital position  $\mathbf{R}_i$ , and the debris orbital velocity  $\mathbf{V}_i$  also shown.

A simplified arm-links model – modified from the work by Shan and Shi [43] such that (i) the masses of the arms in the simplified model are lumped with the MUs and central mass (instead of being continuously

<sup>1</sup> In this work, the RESTORE system's robustness to variation in the target position is analyzed for the maneuver of the Envelopment Phase (see Section 4.2).

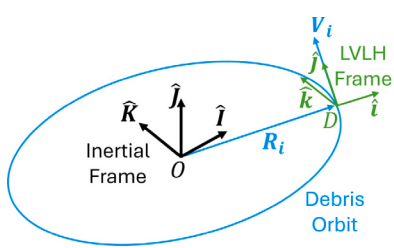


**Fig. 2.** The LVLH frame defined for the analysis of the close rendezvous and final approach phase.

distributed along their lengths) and (ii) the system's dynamics is non-planar – is used for the study of this mission phase and is visualized in **Fig. 3**. For this model, each MU is linked to the central mass through a spring-damper pair (arranged in parallel) that does not exert force in compression. The use of a simplified net model is motivated by the fact that the observed differences between it and the full-net model are relatively small for the maneuvers of Phase I (as will be discussed further in Section 4.1), with simulations with the simplified net model requiring a much lower computational cost due to the lower degrees of freedom present.

Newton's second law can be written for each  $\gamma$ th MU and the central mass as:

$$m_\gamma (\overset{D}{\mathbf{a}}_{\gamma/D}) = \mathbf{T}_\gamma + \mathbf{F}_{I,\gamma} + \mathbf{F}_{T,\gamma} \quad (1)$$

$$m_C (\overset{D}{\mathbf{a}}_{C/D}) = \mathbf{F}_{I,C} - \sum_{\gamma=1}^4 \mathbf{T}_\gamma \quad (2)$$

where  $\mathbf{T}_\gamma$ ,  $\mathbf{F}_{I,\gamma}$ , and  $\mathbf{F}_{T,\gamma}$  represent the tension in the  $\gamma$ th arm, the fictitious force due to the non-inertial LVLH frame, and the applied control force, respectively. The variables  $m_\gamma$  and  $m_C$  are the masses of the  $\gamma$ th MU and of the central mass representing the net, respectively. It should be noted that the mass of each MU decreases over time with consumption of its fuel, which is described by:

$$m_\gamma(t) = m_{MU,0} - \int_0^t \frac{\|\mathbf{F}_{T,\gamma}(\tau)\|}{g_e I_{sp}} d\tau \quad (3)$$

where  $m_{MU,0}$  is the mass of the  $\gamma$ th MU at the beginning of the maneuver,  $g_e = 9.81 \text{ m/s}^2$  is the standard gravitational acceleration of the Earth at sea-level, and  $I_{sp}$  is the specific impulse of the engine. The forces  $\mathbf{T}_\gamma$ ,  $\mathbf{F}_{I,\gamma}$ , and  $\mathbf{F}_{I,C}$  depend on the state of the system and on the  $i$ th debris' orbit and are computed as:

$$\mathbf{T}_\gamma = \begin{cases} T_\gamma \mathbf{e}_\gamma & \text{if } (l_\gamma > l_{\gamma,0}) \\ \mathbf{0} & \text{if } (l_\gamma \leq l_{\gamma,0}) \end{cases} \quad (4)$$

$$\mathbf{F}_{I,\gamma} = m_\gamma (3n_{D,i}^2 x_\gamma + 2n_{D,i} \dot{y}_\gamma) \hat{\mathbf{i}} - 2m_\gamma n_{D,i} \dot{x}_\gamma \hat{\mathbf{j}} - m_\gamma n_{D,i}^2 z_\gamma \hat{\mathbf{k}} \quad (5)$$

$$\mathbf{F}_{I,C} = m_C (3n_{D,i}^2 x_C + 2n_{D,i} \dot{y}_C) \hat{\mathbf{i}} - 2m_C n_{D,i} \dot{x}_C \hat{\mathbf{j}} - m_C n_{D,i}^2 z_C \hat{\mathbf{k}} \quad (6)$$

The variable  $\mathbf{e}_\gamma = \mathbf{r}_{C/\gamma}/l_\gamma$  represents the axial unit vector along the arm direction, computed based on the position of the central mass  $C$  with respect to the  $\gamma$ th MU,  $\mathbf{r}_{C/\gamma}$ , and  $l_\gamma = \|\mathbf{r}_{C/\gamma}\|$ . The tension magnitude  $T_\gamma$  is determined as  $T_\gamma = k_{a,\gamma}(l_\gamma - l_{\gamma,0}) + c_{a,\gamma}v_{r,\gamma}$ , where  $v_{r,\gamma} = \mathbf{r}_{C/\gamma} \cdot (\overset{D}{\mathbf{v}}_{C/\gamma})/l_\gamma$  is the length rate of change of each arm, computed based on  $\overset{D}{\mathbf{v}}_{C/\gamma}$ , the time derivative of  $\mathbf{r}_{C/\gamma}$  with respect to the  $D$  frame. The nominal arm length is computed based on the properties of the actual net as  $l_{\gamma,0} = 0.5L_{\text{side}}\sqrt{2} + l_{ct,0}$ , where  $L_{\text{side}}$  is the net proper side length and  $l_{ct,0}$  is the corner thread length. As noted by the researchers who first formulated the simplified model, there is no analytical expression that

accurately equates the axial stiffness of the arm-links  $k_{a,\gamma}$  to that of an equivalent net [43]. Therefore, this work approximates the axial stiffness and damping coefficients of the simplified model as  $k_{a,\gamma} = EA_{ct}/l_{\gamma,0}$  (where  $A_{ct} = \pi r_{ct}^2$  is the cross-section area of the corner threads) and  $c_\gamma = 2m_{MU,0}\zeta\sqrt{k_\gamma/m_{MU,0}}$  (where  $\zeta$  is the damping ratio). In future work, an optimization-based approach – such as the framework employed by Boonrath et al. [44] to identify parameters of a tethered satellite system – may be used to identify the parameters of the arm-links such that the simplified system dynamics best match that of the full-net model; however, this is outside the scope of this preliminary mission analysis.

In Phase I, the control forces for both the Close Rendezvous and Final Approach maneuvers are determined through a path-tracking PD controller. For each MU, the path the PD controller tracks is based on a minimum-energy solution for a *reference MU model without the net attached* to travel from a set initial state to a desired final state within a given maneuver time  $t_{rnd,i}$  assigned for the  $i$ th debris (where “rnd” in the subscript is the abbreviation of “rendezvous”). In the defined reference model, each MU is simply an independent satellite, where the only applied non-propulsive force is the fictitious force due to the non-inertial nature of LVLH frame; therefore, the dynamics of the reference model is linear and is expressed as follows:

$$\dot{\mathbf{s}}_{m,\gamma}(t) = A_{m,\gamma} \mathbf{s}_{m,\gamma}(t) + B_{m,\gamma} \mathbf{u}_\gamma^*(t) \quad (7)$$

where  $\dot{\mathbf{s}}_{m,\gamma}(t) = [\overset{D}{\mathbf{v}}_{m,\gamma/D}(t), \overset{D}{\mathbf{a}}_{m,\gamma/D}(t)]^T$  is the time derivative of the state vector of the reference model,  $\mathbf{s}_{m,\gamma}(t) = [\mathbf{r}_{m,\gamma/D}(t), \overset{D}{\mathbf{v}}_{m,\gamma/D}(t)]^T$  is the state vector of the reference model,  $A_{m,\gamma}$  is the state matrix of the reference model,  $B_{m,\gamma}$  is the control matrix of the reference model, and  $\mathbf{u}_\gamma^*(t)$  is the minimum-energy control of the reference model. The reference model's  $A_{m,\gamma}$  and  $B_{m,\gamma}$  matrices are defined as follows:

$$A_{m,\gamma} = \begin{bmatrix} 0 & 0 & 0 & 1 & 0 & 0 \\ 0 & 0 & 0 & 0 & 1 & 0 \\ 0 & 0 & 0 & 0 & 0 & 1 \\ 3n_{D,i}^2 & 0 & 0 & 0 & 2n_{D,i} & 0 \\ 0 & 0 & 0 & -2n_{D,i} & 0 & 0 \\ 0 & 0 & -n_{D,i}^2 & 0 & 0 & 0 \end{bmatrix}, \quad B_{m,\gamma} = \begin{bmatrix} 0 & 0 & 0 \\ 0 & 0 & 0 \\ 0 & 0 & 0 \\ 1 & 0 & 0 \\ 0 & 1 & 0 \\ 0 & 0 & 1 \end{bmatrix} \quad (8)$$

Based on the linear reference model dynamics, the minimum-energy control input is computed as:

$$\mathbf{u}_\gamma^*(t) = -B_{m,\gamma}^T e^{A_{m,\gamma}^T(t_0-t)} W^{-1} [\mathbf{s}_{m,\gamma,0} - e^{A_{m,\gamma}(t_0-t_{rnd,i})} \mathbf{s}_{m,\gamma,\text{rnd}}] \quad (9)$$

where  $W = \int_{t_0}^{t_{rnd,i}} e^{A_{m,\gamma}(t_0-\tau)} B_{m,\gamma} B_{m,\gamma}^T e^{A_{m,\gamma}(\tau-t)} d\tau$  is the controllability Grammian of the system,  $\mathbf{s}_{m,\gamma,0}$  is the initial position of the  $\gamma$ th MU, and  $\mathbf{s}_{m,\gamma,\text{rnd}}$  is the desired final position of the  $\gamma$ th MU at the end of each maneuver. Note that each  $\gamma$ th MU is assigned unique  $\mathbf{s}_{m,\gamma,0}$  and  $\mathbf{s}_{m,\gamma,\text{rnd}}$  such that the threads are almost at their natural lengths at the beginning and the end of the maneuvers, respectively (example sets of initial states and final desired states can be seen in Section 4.1). At the end of the Close Approach and at the beginning of the Final Rendezvous maneuvers, the desired speeds of the RESTORE system relative to the debris are set to zero to facilitate its arrival and departure from the holding position, respectively.

Given the reference control and dynamics for each MU, the actual applied control force and the associated fuel consumption throughout each stage of Phase I are computed as:

$$\mathbf{F}_{T,\gamma}(t) = K_P(\mathbf{r}_{m,\gamma/D}(t) - \mathbf{r}_{\gamma/D}(t)) + K_D(\overset{D}{\mathbf{v}}_{m,\gamma/D}(t) - \overset{D}{\mathbf{v}}_{\gamma/D}(t)) \quad (10)$$

$$m_{\text{prop},\text{rnd},i} = \sum_{\gamma=1}^4 \int_0^{t_{rnd,i}} \frac{\|\mathbf{F}_{T,\gamma}(\tau)\|}{g_e I_{sp}} d\tau \quad (11)$$

with  $\mathbf{r}_{\gamma/D}(t)$  and  $\overset{D}{\mathbf{v}}_{\gamma/D}(t)$  representing the actual position and velocity of the  $\gamma$ th MU with respect to the debris. The variables  $K_P$  and  $K_D$  indicate the proportional and derivative gains of the PD controller, respectively. To represent the change in the system's speed due to the

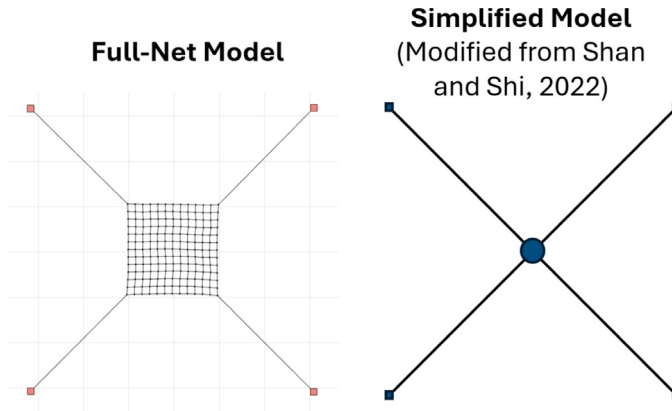


**Fig. 3.** Simplified net system for close rendezvous and final approach analyses. The simplified system model was modified from [43].

applied thrusts, the average  $\Delta v_{\text{rnd},i}$  used by the MUs for the maneuver is computed as:

$$\Delta v_{\text{rnd},i} = 0.25 \sum_{\gamma=1}^4 \int_0^{t_{\text{rnd},i}} \frac{\|\mathbf{F}_{T,\gamma}(\tau)\|}{m_\gamma(\tau)} d\tau \quad (12)$$

### 3.2. Phase II: Envelopment

To study the envelopment phase, a high-fidelity model of the net – with the actual net mesh present – is required such that the contact dynamics of the RESTORE system with the debris can be represented. The high-fidelity model is implemented within Vortex Studio,<sup>2</sup> a multi-body dynamics simulation framework, building upon prior work by Botta et al. [6]. We adopt a lumped-parameter modeling approach, one of the most popular and computationally efficient models for space net systems [6,9,11,36]. The lumped-parameter model lumps the continuously distributed mass of the net threads into small spherical rigid bodies, called *nodes*. The nodes are connected at their CoMs via massless nonlinear spring-damper elements (representing the elastic nature of their materials) into a grid-like pattern to form the net mesh. As the attitude motion of the MUs are not considered in this work, the nonlinear spring-damper elements are also connected at the CoMs of the MUs. A scaled-box friction model and a continuous compliant contact force model are employed to compute the contact forces. Such lumped parameter models and continuous compliant contact dynamics formulations have been validated by multiple researchers in the past [26,45].

Due to the fact that the RESTORE system is in contact with the debris throughout Phase II (and therefore influences its orbit such that it is no longer circular), the CWH equations are no longer viable to represent relative dynamics. Instead, both the spacecraft and the debris are subject to gravitational accelerations according to the two-body model: for each body (i.e., debris, MUs, and nodes of the net), the gravitational force  $\mathbf{F}_G$  is applied to the CoM as an external force in the equations of motion:

$$\mathbf{F}_G(t) = -m\mu \frac{\mathbf{R}(t)}{\|\mathbf{R}(t)\|^3} \quad (13)$$

where  $\mathbf{R}$  is the orbital position of each body's CoM and  $m$  is the mass of each body. For the sake of conciseness, the equations of motion are not reported for the high-fidelity model; instead, interested readers can refer to prior works by the authors [6,32] for detailed formulation.

Similar to Phase I, a PD path-tracking control is used to control the position of the RESTORE system. As contact forces between the system and target are present throughout the envelopment, it is foreseen that the true dynamics of the MUs will deviate much more from the linear reference model employed in the previous mission phase. Accordingly, a straight-line path – inspired by the formulation proposed by Boonrath et al. [16] for guiding the deployment of tethered SNRs – is defined for each MU to track throughout Phase II:

$$\mathbf{r}_{d,\gamma}(t) = \mathbf{r}_{0,\gamma} + (\alpha_{\text{env},1} t + \alpha_{\text{env},2} t^2) (\mathbf{r}_{\text{env},\gamma} - \mathbf{r}_{0,\gamma}) \quad (14)$$

where  $\mathbf{r}_{d,\gamma}(t)$  is the desired position of the  $\gamma$ th MU at time  $t$ ,  $\mathbf{r}_{0,\gamma}$  is the initial position of the  $\gamma$ th MU at the beginning of the envelopment, and  $\mathbf{r}_{\text{env},\gamma}$  is the desired final position of the  $\gamma$ th MU at the end of the envelopment. The final position  $\mathbf{r}_{\text{env},\gamma}$  is user-defined (with examples shown in Section 4.2), but in general is behind the target in the along-track direction. The position vectors in Eq. (14) are expressed in the frame  $\mathcal{E} = \{E, \hat{\mathbf{e}}_x, \hat{\mathbf{e}}_y, \hat{\mathbf{e}}_z\}$ , which is centered at (i.e., orbits along with) the CoM of the debris as if the envelopment maneuver did not occur. This frame definition was chosen to allow the RESTORE system to use a reference frame independent of its motion (which would not have been if  $E$  was fixed to the actual debris CoM) for guidance during the envelopment maneuver. The directions  $\{\hat{\mathbf{e}}_x, \hat{\mathbf{e}}_y, \hat{\mathbf{e}}_z\}$  of the  $\mathcal{E}$  frame represent the radial, along-track, and cross-track directions of the orbit, respectively. The axes of the  $\mathcal{E}$  frame and the final desired positions for the MUs are displayed in Fig. 4. The variables  $\alpha_{\text{env},1}$  (with a unit of 1/s) and  $\alpha_{\text{env},2}$  (with a unit of 1/s<sup>2</sup>) in Eq. (14) are positive constants used to adjust the desired velocities of the MUs with respect to the  $\mathcal{E}$  frame:

$${}^{\mathcal{E}}\mathbf{v}_{d,\gamma}(t) = (\alpha_{\text{env},1} + 2\alpha_{\text{env},2}t) (\mathbf{r}_{\text{env},\gamma} - \mathbf{r}_{0,\gamma}) \quad (15)$$

In general, these constants should be computed such that each MU reaches its desired final position  $\mathbf{r}_{\text{env},\gamma}$  by the user-defined duration of each envelopment maneuver  $t_{\text{env},i}$  (an example set of constants is later provided in Section 4.2). The increasing desired velocity magnitude – due to the positive  $(\alpha_{\text{env},1} + 2\alpha_{\text{env},2}t)$  term of Eq. (15) – is designed to facilitate debris trapping, as the accelerating motion of the RESTORE system with respect to the  $\mathcal{E}$  frame is expected to promote sustained contact of the debris with the net throughout the envelopment. To compute the control force applied onto each MU in Phase II, Eq. (10) is used with  $\mathbf{r}_{m,\gamma/D}(t)$  replaced by  $\mathbf{r}_{d,\gamma}(t)$  for the path-tracking scheme, while the desired velocity is set to  ${}^{\mathcal{E}}\mathbf{v}_{d,\gamma}(t)$ . The costs  $m_{\text{prop},\text{env},i}$  and  $\Delta v_{\text{env},i}$  are computed using Eqs. (11) and (12), respectively, with  $t_{\text{rnd},i}$  replaced by  $t_{\text{env},i}$ .

<sup>2</sup> Vortex Studio is developed by the CM Labs Simulations Inc. and is available for research use.

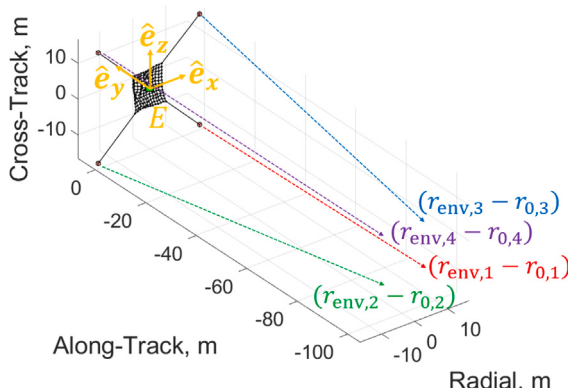


Fig. 4. The  $\mathcal{E}$  frame and the final desired positions for the MUs in Phase II.

### 3.3. Phase III: Dragging

In Phase III, the RESTORE system drags each debris – along the direction opposite to the orbital velocity – to lower the orbital speed of the coupled system. The dragging maneuver is required since the ejection maneuver is not expected to impart the entire  $\Delta v_{\text{deo},i}$  (that is, the total change in the orbital speed required for deorbiting) to each  $i$ th debris.<sup>3</sup> In Phase III, the RESTORE system is set to lower the orbital speed of each debris by  $\Delta v_{\text{drag},i} = (p_{\text{drag}}/100)\Delta v_{\text{deo},i}$ , where  $p_{\text{drag}}$  is the  $\Delta v$  percent contribution of the dragging maneuver towards the total required orbital speed reduction. The quantity  $p_{\text{drag}}$  is determined for each debris based on the total  $\Delta v$  required for deorbiting and the speed change that the RESTORE system is able to induce onto the debris via the ejection maneuver (see Section 5 for example computations of the value within debris removal missions.)

For the study of this Phase, it is assumed there is no relative motion between the RESTORE system and the debris trapped inside; therefore, the bodies are modeled together as a single lumped point-mass subject to gravitational accelerations according to the two-body model (see Eq. (13)). With this model, the  $\Delta v_{\text{deo},i}$  required for an impulsive, Hohmann-like maneuver can be computed for each  $i$ th debris (with orbital radius  $R_i$ ) as follows:

$$\Delta v_{\text{deo},i} = \left| \sqrt{\frac{\mu}{R_i}} - \sqrt{2\mu \left( \frac{1}{R_i} - \frac{1}{2a_{\text{deo},i}} \right)} \right| \quad (16)$$

where  $a_{\text{deo},i} = ((h_{\text{deo}} + R_{\oplus}) + R_i)/2$  and  $R_{\oplus} = 6378$  km is the nominal radius of the Earth. Accordingly, Tsiolkovsky's rocket equation can be used to compute consumed fuel mass  $m_{\text{prop,drag},i}$  required for Phase III:

$$m_{\text{prop,drag},i} = m_{0,\text{drag},i} \left( 1 - e^{-\frac{\Delta v_{\text{drag},i}}{g_e I_{\text{sp}}}} \right) \quad (17)$$

where  $m_{0,\text{drag},i}$  is the combined RESTORE system and debris mass at the start of the dragging maneuver.

### 3.4. Phase IV: Ejection

For the study of Phase IV, many combinations of system design parameters are considered to maximize the debris ejection speed. Because of the large number of numerical simulations required to analyze the designs, the high-fidelity net model is unsuitable for the study of this Phase due to its high computational cost. Therefore, to acquire insight into the effects of control and design parameters on the system dynamics, a computationally-efficient (yet sufficiently accurate) simplified

model of the net-debris system is considered (see Fig. 5).<sup>4</sup> This model is similar to the arm-links model described in Section 3.1, however, some additional simplifications are made. Specifically, due to the very short duration of the ejection phase, gravitational acceleration (which acts almost identically on both the RESTORE system and the debris) is neglected. The dynamics of the simplified model is taken to be planar, as the ejection maneuver is designed to be symmetric such that the dynamics of the MUs are similar in the cross-track and radial directions. Because of this symmetry, only 2 MUs (i.e., bodies  $P$  and  $Q$ ) are present within the planar model. To represent the net and debris being in contact throughout the ejection maneuver, the debris is assumed to be rigidly attached to the RESTORE system's center  $H$ . Right before the ejection maneuver, the RESTORE system is initially configured such that (i) the bodies  $P$ ,  $Q$ , and  $H$  are stationary relative to the  $C$  frame, (ii) the arm-links are stretched to their natural lengths, and (iii) the arm-links are rotated at an angle of  $\psi$  relative to the negative along-track direction. The frame  $C = \{C, \hat{e}_x, \hat{e}_y, \hat{e}_z\}$  is centered at (i.e., orbits along with) the CoM of the debris as if it had not been ejected; this was chosen such that the speed of the debris relative to the  $C$  frame is representative of how much the ejection maneuver changes the debris' orbital speed. The directions  $\{\hat{e}_x, \hat{e}_y, \hat{e}_z\}$  of the  $C$  frame represent the radial, along-track, and cross-track directions of the orbit, respectively. Lastly, the model is assumed to be valid until right before the RESTORE system is fully stretched out (i.e., when the debris is expected to be released from the net's center).

Newton's second law can be written for each body in the planar simplified model as:

$$m_P(C \mathbf{a}_{P/C}) = F_{T,P}(-\cos \phi \hat{e}_y + \sin \phi \hat{e}_x) + T_P(\cos \psi \hat{e}_y - \sin \psi \hat{e}_x) \quad (18a)$$

$$m_H(C \mathbf{a}_{H/C}) = -T_P(\cos \psi \hat{e}_y - \sin \psi \hat{e}_x) - T_Q(\cos \psi \hat{e}_y + \sin \psi \hat{e}_x) \quad (18b)$$

$$m_Q(C \mathbf{a}_{Q/C}) = F_{T,Q}(-\cos \phi \hat{e}_y - \sin \phi \hat{e}_x) + T_Q(\cos \psi \hat{e}_y + \sin \psi \hat{e}_x) \quad (18c)$$

For the equations above, the discontinuous spring-damper model is again adopted to describe the dynamics of the arm-links, where the tension magnitudes  $T_P$  and  $T_Q$  are described by Eq. (4). It should be noted that the length of each arm-link can vary over time, as the model allows it to be greater or smaller than its natural length. The applied thrusts are set to have equal and constant magnitudes of  $F_{T,P} = F_{T,Q} = F_T$ . It is assumed that the propulsion system maintains a constant thrust angle  $\phi$  throughout the ejection. The masses  $m_P = m_Q = 2m_{\text{MU}} + 0.25m_{\text{net}}$  are of 2 MUs and a portion of the net lumped into points  $P$  and  $Q$ , while the mass  $m_H = m_D + 0.5m_{\text{net}}$  is of the debris and a portion of the net lumped at the center  $H$ . Similar to the model used for the analysis of Phase I,  $m_P$  and  $m_Q$  decrease over time depending on the histories of applied thrusts, in accordance with Eq. (11). The unstretched arm length is computed as  $l_{\xi,0} = 0.5L_{\text{side}} + l_{ct,0}$ , while the stiffness and damping properties of the system are computed in the same manner as in Section 3.1.

Given the assumption that the MUs maneuver symmetrically (i.e., that points  $P$  and  $Q$  move symmetrically about the  $\hat{e}_y$  axis), the planar model described by Eq. (18) possesses three degrees of freedom (DoF). Therefore, to describe the dynamics of the RESTORE system during the ejection phase, the following three scalar differential equations must be solved:

$$m_P \ddot{x}_P = F_T \sin \phi - T \sin \psi \quad (19a)$$

$$m_P \ddot{y}_P = -F_T \cos \phi + T \cos \psi \quad (19b)$$

$$m_H \ddot{y}_H = -2T \cos \psi \quad (19c)$$

where  $T = T_P = T_Q$  is the tension magnitude in each of the arm-links. Variables  $\dot{x}_P$  and  $\dot{y}_P$  are components of the acceleration of point  $P$

<sup>3</sup> See Section 4.3 for an in-depth discussion on the imparted  $\Delta v$  limitation of the ejection maneuver.

<sup>4</sup> The dynamics of the simplified model is validated against sample ejection scenarios simulated using the high-fidelity model (see the discussions of Section 4.3.3)

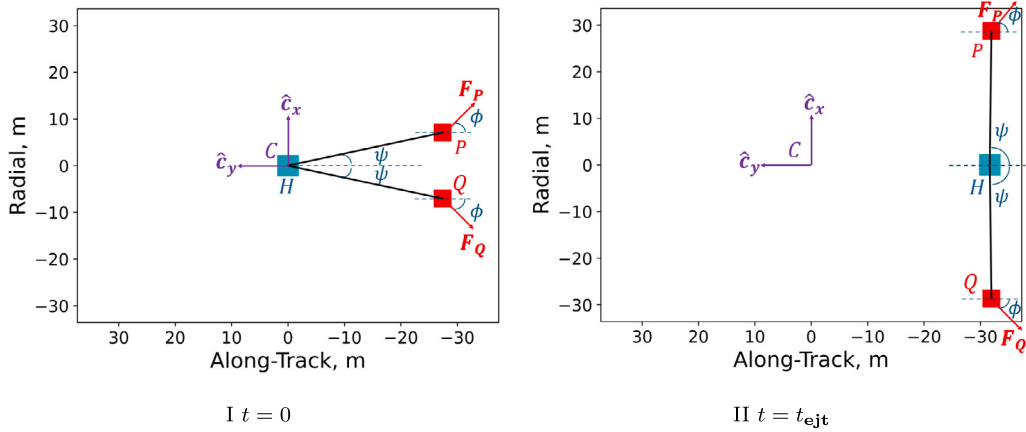


**Fig. 5.** Simplified net-debris system for Phase IV (a) at the beginning and (b) at the end of the maneuver.

with respect to the  $C$  frame, while  $\dot{y}_H$  is the along-track component of the acceleration of point  $H$  with respect to the same frame. The fuel consumed by the end of the ejection maneuver is

$$m_{\text{prop,ejt},i} = \int_0^{t_{\text{ejt},i}} \frac{2F_T}{g_e I_{\text{sp}}} d\tau = \frac{2F_T t_{\text{ejt},i}}{g_e I_{\text{sp}}} \quad (20)$$

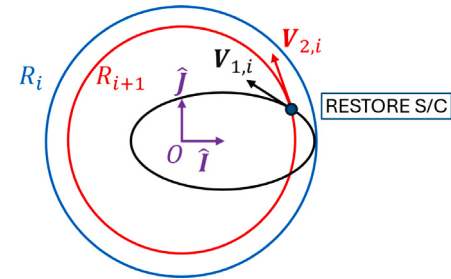
where  $t_{\text{ejt},i}$  is the duration of the ejection maneuver for the  $i$ th debris.

### 3.5. Phase V: Relocation and phasing

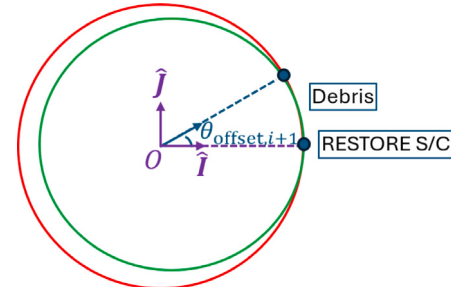
After Phase IV, RESTORE relocates and maneuvers to the phase of the next debris and repeats the entire process of trapping and ejection till it runs out of fuel. We use classical orbital mechanics to approximately compute the required changes to the system's orbital speed and the corresponding fuel consumption, and model the spacecraft as a single lumped point-mass subject to gravitational accelerations according to the two-body model (see Eq. (13)). Orbital maneuvers in this Phase are assumed to be impulsive.

Fig. 6 displays a diagram of the relocation process, where the larger blue circular orbit (with radius  $R_i$ ) represents the original orbit of the deorbited debris, the black elliptical orbit represents the orbit the RESTORE system is on after the completion of Phase IV, and the red circular orbit (with radius  $R_{i+1}$ ) represents the orbit of the next debris. The variables  $V_{1,i}$  and  $V_{2,i}$  represent the inertial velocities of the RESTORE system with respect to the Earth-centered inertial frame  $\mathcal{O}$  right before and after the impulsive thrust application. Assuming that the impulsive thrust application occurs at the intersection of the elliptical transfer orbit and the orbit of the  $(i+1)$ th debris (as seen in Fig. 6), the cost of the relocation maneuver  $\Delta v_{\text{reo},i}$  is determined through the use of analytical expressions for an impulsive non-Hohmann transfer [46]. Accordingly, the fuel mass consumed by the RESTORE system for the relocation maneuver,  $m_{\text{prop,reo},i}$ , is computed via Eq. (17) with  $\Delta v_{\text{drag},i}$  and  $m_{0,\text{drag},i}$  replaced by  $\Delta v_{\text{reo},i}$  and  $m_{0,\text{reo},i}$  (i.e., the system's total mass right before the relocation maneuver), respectively.

After the RESTORE system is in the same orbit as the next debris targeted for removal, a phasing maneuver is performed to catch up to the debris. Fig. 7 displays the diagram of the phasing process, where the debris and spacecraft are assumed to have an initial true anomaly offset of  $\theta_{\text{offset},i+1}$ . Within the figure, the red orbit represents the initial RESTORE system orbit, and the green orbit represents the phasing orbit. The phasing maneuver cost  $\Delta v_{\text{p},i}$  can be determined analytically for a two-impulse phasing maneuver [46]. The fuel mass consumed by the RESTORE system for the phasing maneuver,  $m_{\text{prop,p},i}$ , is computed via Eq. (17) with  $\Delta v_{\text{drag},i}$  and  $m_{0,\text{drag},i}$  replaced by  $\Delta v_{\text{p},i}$  and  $m_{0,\text{p},i}$  (i.e., the system's total mass right before the phasing maneuver), respectively.



**Fig. 6.** Diagram of the relocation process. (For interpretation of the references to color in this figure legend, the reader is referred to the web version of this article.)



**Fig. 7.** Diagram of the phasing process. (For interpretation of the references to color in this figure legend, the reader is referred to the web version of this article.)

## 4. Numerical analyses of the rendezvous, envelopment, and ejection phases

This Section presents the numerical analysis of results from simulations performed for the Rendezvous, Envelopment, and Ejection phases of the mission. Unlike the Dragging and Relocation and Phasing phases, where the  $\Delta v$  and fuel costs can be computed analytically (see Sections 3.3 and 3.5 for the associated justifications and assumptions, respectively), these three phases are modeled numerically; accordingly, we assess the performance and fidelity of the proposed models and control schemes through numerical experiments. Moreover, in Phases I and IV, the results obtained with the simplified models of the net are compared against a higher-fidelity lumped-parameter net model simulation. In Phase IV, we also use the high-fidelity net mode to

**Table 1**

Physical properties of the RESTORE system.

Parameter	Value
Net side length $L_{\text{side}}$ , m	10.0
Net mesh length $l_{\text{net},0}$ , m	0.833
Net proper thread radius $r_{\text{net}}$ , m	0.0005
Net proper and corner thread density $\rho$ , kg/m <sup>3</sup>	1390
Net proper and corner thread young's modulus $E$ , GPa	70
Net proper and corner thread damping ratio $\zeta$ , –	0.106
Corner thread length $l_{\text{ct},0}$ , m	15
Corner thread radius $r_{\text{ct}}$ , m	0.001
MU mass $m_{\text{MU}}$ , kg	3.5

verify whether the maximum tension experienced by the RESTORE system in the structurally-demanding ejection process remains under the maximum tensile limit of the threads.

All simulations use the design parameters presented in [Table 1](#), while the contact properties of the lumped-parameter net are computed in accordance to Ref. [47]. The initial mass of each MU, of 3.5 kg, is set such that it is below the 4.0 kg limit for 2U-Cubesats [33], while the mass of the net proper,  $m_{\text{net}}$ , is computed to be 0.54 kg based on the net's geometry and material properties [47]. Each MU is assumed to be equipped with a chemical rocket propulsion system, with a thrust saturation limit of 22 N [48], to control its motion. For the study of Phases II and III, two debris masses of  $m_D = 0.5$  kg and  $m_D = 3.0$  kg are considered to examine the performance of the proposed control schemes under multiple conditions. In Phase II, both debris (cuboid in shape) are set to have initial rotation speeds of approximately 29°/s (within the range of observed rotation speeds of actual debris [49]). All debris objects in the case studies of this Section are located on a circular orbit at an altitude of 780 km above the Earth's surface.

#### 4.1. Numerical study of phase I: Close rendezvous and final approach

First, we examine the dynamics of the simplified model proposed in [Section 3.1](#). The system's dynamics in both the Final Approach and Close Rendezvous stages were observed to be very similar; accordingly, we only show the simulation results for the Final Approach stage of Phase I. With the state of the  $y$ th MU represented as  $s_y(t) = [\mathbf{r}_{y/D}(t), {}^D \mathbf{v}_{y/D}(t)]^T$ , the initial conditions (in m and m/s) for each MU and central mass are symmetrically defined as:

$$\mathbf{s}_y(0) = [\pm 15.45, -300, \pm 15.45, 0, 0, 0]^T_D \quad (21a)$$

$$\mathbf{s}_C(0) = [0, -300, 0, 0, 0, 0]^T_D \quad (21b)$$

The initial states of each MU's linear reference model are set to be identical to the initial states of the corresponding actual MU (i.e.,  $\mathbf{s}_{m,y,0} = \mathbf{s}_y(0)$ ). The desired final state at  $t_{\text{rnd}} = 1600$  s for each MU – with a final approach speed of  $v_{f,\text{rnd}}$  – is symmetrically defined as:

$$\mathbf{s}_{m,y,\text{rnd}}(t_{\text{rnd}}) = [\pm 15.45, 0, \pm 15.45, 0, -v_{f,\text{rnd}}, 0]^T_D \quad (22)$$

We impose a non-zero final speed, as the RESTORE system will need to perform the envelopment maneuver – where each MU flies past the CoM of the debris to enclose it within the net proper – right after Phase I is completed. The gains for the PD controller are heuristically tuned and selected as  $K_P = 100$  N/m and  $K_D = 50$  N s/m, respectively, for the simulations of this Phase.

The resulting trajectory for the Final Approach stage is shown in [Fig. 8\(I\)](#), where the path of the RESTORE system can be seen traveling from a holding position 300 m behind the debris (in the along-track direction) to a position right in front of it. This maneuver is chosen to allow the RESTORE system to initiate the envelopment maneuver (i.e., Phase II) from the front of the debris and then enable a smooth transition to the subsequent dragging phase (i.e., Phase III). [Fig. 8\(II\)](#) displays the tracking error between the reference positions and the actual positions of the 4 MUs; it can be seen that the errors are minimal

for most of the flight, indicating that the tension forces acting on the MUs are sufficiently small for the PD controller to overcome, allowing the RESTORE system to track the desired trajectory. We also compared the positions of the MUs in the simplified arm-links model against those obtained with the high-fidelity lumped-parameter net model (simulated with the same initial conditions, applied CWH forces, and control law described in [Section 3.1](#)); the differences are less than  $1 \times 10^{-4}$  m throughout the entire maneuver, showing that the simplified model is sufficiently accurate in simulating the MUs dynamics within Phase IV. For this Final Approach scenario, it was found that the maximum thrust magnitude required for the control of the MUs during the maneuver, of approx. 0.0048 N, is minimal compared to the control saturation limit, of 22 N. All MUs combined were also found to only consume approximately 5.1 g of fuel for the maneuver. Interested readers may refer to [Appendix A](#) for additional results concerning time histories of the applied thrusts and fuel consumed for the MUs, as well as a study on how the final time  $t_{\text{rnd}}$  and the desired final speed for each MU  $v_{f,\text{rnd}}$  affect fuel consumption.

#### 4.2. Numerical study of phase II: Envelopment

This subsection examines the ability of the guidance scheme defined in [Section 3.2](#) to conduct the envelopment maneuver. The initial position (in m) for each MU in the  $\mathcal{E}$  frame – based on the system's final configuration at the end of Phase I such that the net is almost fully stretched out – is set to be the following:

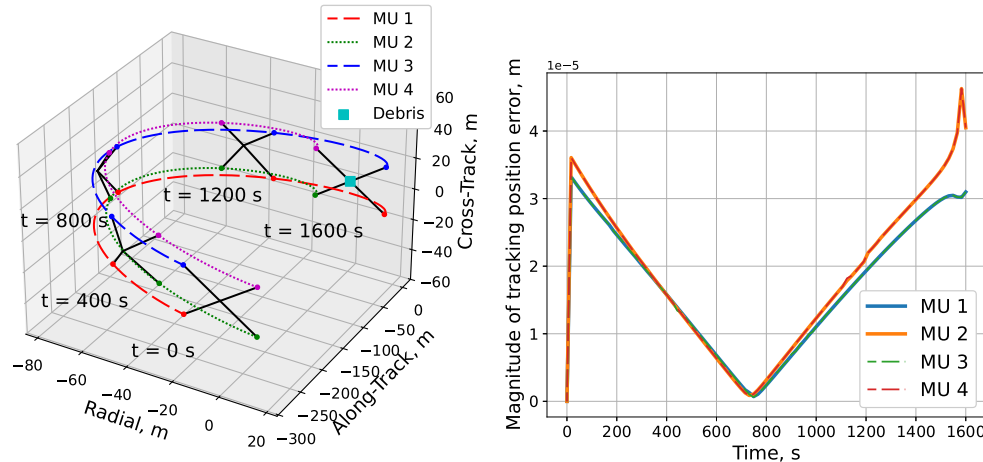
$$\mathbf{r}_{0,y} = [\pm 15.45, 0, \pm 15.45]^T_{\mathcal{E}} \quad (23)$$

The desired final positions (in m) for the MUs – required by the path-tracking PD control – are defined symmetrically as:

$$\mathbf{r}_{\text{env},y} = [\pm 5.0, -100, \pm 5.0]^T_{\mathcal{E}} \quad (24)$$

This choice of final desired positions commands the MUs to move closer together in the radial and cross-track directions, while simultaneously slowly dragging the debris along the negative along-track direction. We empirically selected a maneuver time of  $t_{\text{env}} = 30$  s for the sample debris envelopment simulation. For the desired position and velocities (per Eqs. (14) and (15)), the variables  $\alpha_{\text{env},1}$  and  $\alpha_{\text{env},2}$  are selected as 0.0153 1/s and 0.0006 1/s<sup>2</sup>, respectively, such that each MU travels from  $\mathbf{r}_{0,y}$  to  $\mathbf{r}_{\text{env},y}$  approximately within  $t_{\text{env}}$ . The gains for the PD controller were heuristically tuned as  $K_P = 15$  N/m and  $K_D = 5$  N s/m for this phase.

For the analysis of Phase II, two scenarios are considered, each employing debris with masses of  $m_D = 3.0$  and 0.5 kg. In the nominal scenario, the debris is initially positioned such that it is located on the center of the RESTORE system (see [Fig. 9\(I\)](#)), while in the non-nominal scenario, the debris is initially positioned such that its CoM is offset from the net's CoM by 3 m in the radial direction (see [Fig. 9\(II\)](#)). The misalignment of the net and the debris may be the result of imperfect sensing and actuation capabilities within a real mission; accordingly, the non-nominal scenario represents a case study where conditions are not ideal for the RESTORE system. As seen in [Fig. 9\(I\)](#), which displays snapshots taken throughout the high-fidelity simulation of Phase II, the system is able to perform the envelopment maneuver successfully in the nominal scenario. The defined maneuver plan was found to be successful with debris masses of  $m_D = 3.0$  kg (the case shown in [Fig. 9\(I\)](#)) and  $m_D = 0.5$  kg, indicating that the proposed guidance scheme and control are robust to some degree of debris parameter variations. The maximum thrust required for the maneuver (of approximately 12 N per each MU for both the considered debris masses) and the corresponding fuel consumed for the entire maneuver (of approximately 0.010 kg and 0.013 kg per MU for  $m_D = 0.5$  kg and  $m_D = 3.0$  kg, respectively) are relatively low. In the non-nominal scenario, the RESTORE system is again successful in performing the envelopment maneuver for debris with masses of  $m_D = 3.0$  kg (the case shown in [Fig. 9\(II\)](#)) and  $m_D = 0.5$  kg, indicating that the system is



I 3D maneuver path.

II MUs tracking position error.

Fig. 8. Plots concerning the final approach maneuver.

robust to offset in the debris relative position in the radial direction. It is interesting to note that even though the CoMs of the net and the debris are initially misaligned in Fig. 9(II), by the end of the envelopment at  $t = 30$  s, the debris is approximately located at the center of the system. It is also found that the maximum thrust required and the total fuel consumed are nearly identical in the nominal and non-nominal scenarios. Therefore, it is shown that the proposed maneuver scheme has sufficient performance to conduct the envelopment of the debris, even without an ideal initial net-debris alignment. The limitation of the proposed control scheme (e.g., the upper debris mass limit beyond which the path-tracking PD control would no longer work) is left to be a topic of analysis within future work.

#### 4.3. Numerical study of phase IV: Ejection

##### 4.3.1. Effects of varying system parameters on the ejection dynamics

For the analysis of the Phase IV, we first study the effects of varying the system parameters and the applied control on the debris ejection using the planar simplified model of the net-debris system presented in Section 3.4. Phase IV is vital for the planning of the ADR mission, as the amount of  $\Delta v$  imparted by the maneuver dictates the remaining amount of debris deorbiting  $\Delta v$  that is required by the dragging phase (i.e.,  $\Delta v_{\text{drag}}$ ). Since the RESTORE system incurs a much lower orbital energy reduction from the ejection maneuver than from the dragging maneuver, maximizing of the debris ejection speed (and therefore minimizing the  $\Delta v_{\text{drag}}$  required) is highly desirable. With this in mind, we study the effects of the control and design parameters defined in Section 3.4 – including  $\psi_0$  (i.e., the initial  $\psi$ ),  $\phi$ ,  $m_D$ ,  $m_{\text{MU},0}$  (i.e., the initial mass of each MU),  $l_{\text{ct},0}$ , and  $F_T$  – on these figures of merit. For all numerical simulations of this section, the simulation end time is set as either the instance when  $\psi = 90^\circ$  (i.e., when the system is flattened-out) or  $t_{\text{ejt,max}} = 15$  s, whichever is less.

The system is first simulated with the angles  $\psi_0$  and  $\phi$  varying; parameters  $F_T = 2 \cdot 22 = 44$  N,  $l_{\text{ct},0} = 15$  m,  $m_D = 0.5$  kg, and  $m_{\text{MU},0} = 3.5$  kg are fixed across scenarios.<sup>5</sup> Fig. 10 displays 3D surface plots of the final debris velocity component in the  $-\hat{\mathbf{c}}_y$  direction (i.e.,  $-\dot{y}_H(t_{\text{ejt}})$ ),

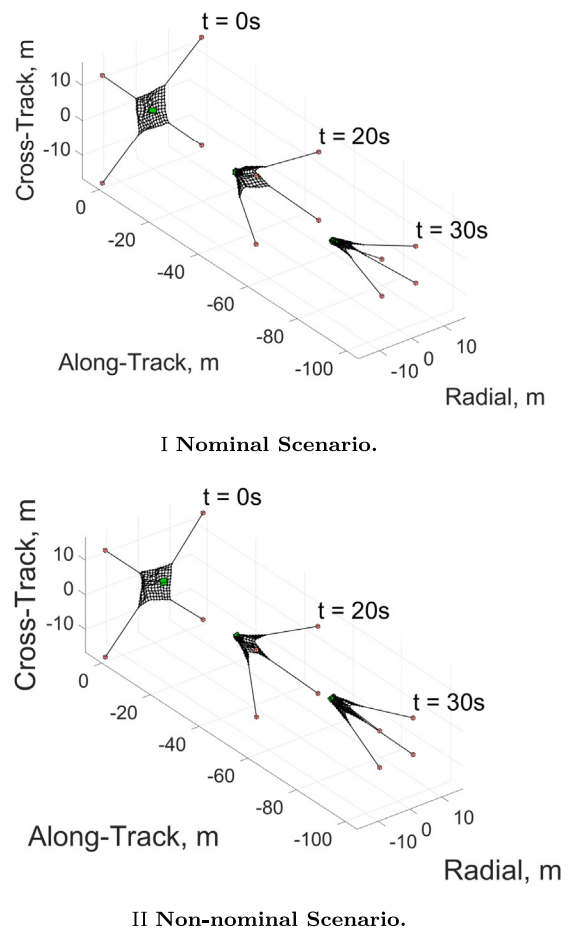


Fig. 9. Snapshots from high-fidelity simulations of Phase II.

<sup>5</sup> Here, the thrust magnitude is set as  $F_T = 2 \cdot 22 = 44$  N due how in the planar model, bodies  $P$  and  $Q$  each represent 2 MUs of the full system (see Section 3.4).

the final RESTORE system's CoM velocity component in the  $-\hat{c}_y$  direction (i.e.,  $-\dot{y}_{\text{CoM}}(t_{\text{ejt}})$ ), and the total fuel consumed (i.e.,  $m_{\text{prop,ejt}}$ ) as functions of the varying angles. Due to ejection symmetry, the magnitudes of  $\dot{y}_H(t_{\text{ejt}})$  and  $\dot{y}_{\text{CoM}}(t_{\text{ejt}})$  are equivalent to the final speeds of the debris and of the RESTORE system's CoM with respect to the  $C$  frame, respectively. The quantity  $\dot{y}_{\text{CoM}}(t)$  is computed as follows:

$$\dot{y}_{\text{CoM}}(t) = \frac{m_P(t)\dot{y}_P(t) + m_Q(t)\dot{y}_Q(t) + m_{\text{net}}\dot{y}_H(t)}{m_P(t) + m_Q(t) + m_{\text{net}}} \quad (25)$$

In Fig. 10(I), we observe that the initial angle  $\psi_0$  has a larger effect on  $-\dot{y}_H(t_{\text{ejt}})$  compared to the thrust angle  $\phi$ . For  $30^\circ \leq \phi \leq 80^\circ$ , relatively little change in  $-\dot{y}_H(t_{\text{ejt}})$  is observed. However, an approximately linear inverse relationship exists between  $-\dot{y}_H(t_{\text{ejt}})$  and  $\psi_0$ . For example, with  $\phi = 80^\circ$ ,  $-\dot{y}_H(t_{\text{ejt}})$  is approximately 60 m/s and 20 m/s for initial  $\psi_0 = 15^\circ$  and  $\psi = 60^\circ$ , respectively. There is a region of exception to this general trend for  $74.58^\circ \leq \psi_0 \leq 80^\circ$  and  $20^\circ \leq \phi \leq 27.5^\circ$ , where the observed  $-\dot{y}_H(t_{\text{ejt}})$  values are noticeably greater than the  $-\dot{y}_H(t_{\text{ejt}})$  values immediately outside of the said region. This phenomenon will be further investigated through the other subplots of Fig. 10.

In Fig. 10(II),  $-\dot{y}_{\text{CoM}}(t_{\text{ejt}})$  is examined for varying  $\psi_0$  and  $\phi$ . A lower  $-\dot{y}_{\text{CoM}}(t_{\text{ejt}})$  is desired as it corresponds to a lower amount of orbit correction the RESTORE system needs to perform after debris ejection. From Fig. 10(II),  $\phi$  must be maximized at  $80^\circ$  to achieve the lowest  $-\dot{y}_{\text{CoM}}(t_{\text{ejt}})$ . Furthermore, it is interesting to note that for high values of  $\phi$  (i.e., above approximately  $70^\circ$ ), the angle  $\psi_0$  has a relatively minor effect on  $-\dot{y}_{\text{CoM}}(t_{\text{ejt}})$ . A region of exception to the general trend is observed here too, where  $-\dot{y}_{\text{CoM}}(t_{\text{ejt}})$  is relatively high with large  $\psi_0$  and small  $\phi$ . In fact,  $-\dot{y}_{\text{CoM}}(t_{\text{ejt}})$  and  $-\dot{y}_H(t_{\text{ejt}})$  are almost the same in that regime; this behavior shows that the debris is dragged by the RESTORE system instead of being ejected when such combinations of parameters are applied to the system.

The fuel consumed for Phase IV of the mission is examined in Fig. 10(III). It should be noted that, because the thrust applied for Phase IV is constant over time, the fuel consumed and the total ejection time are proportionally related (see Eq. (20)). A lower amount of fuel consumed – and therefore lower total time of the ejection maneuver – is desired. To achieve these goals,  $\phi$  must be as high as possible (i.e.,  $80^\circ$  in this study). Even though higher  $\psi_0$  yields smaller fuel consumed and maneuver time,  $\psi_0$  should be selected as a relatively small value to maximize the debris ejection speed, as per Fig. 10(I). In Fig. 10(III), the high amount of fuel consumed, and therefore a long simulation completion time, for large  $\psi_0$  and small  $\phi$  is further evidence that, for such combinations of parameters, the debris is dragged by the RESTORE system rather than being ejected. This is also confirmed by the fact that all the simulations in this region reached the maximum allotted time of  $t_{\text{ejt,max}} = 15$  s, indicating that  $\psi$  never reached  $90^\circ$  in these scenarios; the mathematical cause of this phenomenon will be explored in Section 4.3.2. Outside of the discontinuous region,  $t_{\text{ejt}}$  ranges from approx. 0.9 s to 4.9 s. Overall, according to the results in Fig. 10, it is preferable to employ angles  $\psi_0 = 15^\circ$  and  $\phi = 75^\circ$  for the ejection maneuver.

The system is next simulated with varying  $m_D$  and  $m_{\text{MU},0}$ ; the parameters  $\psi_0 = 15^\circ$ ,  $\phi = 75^\circ$ ,  $F_T = 44$  N, and  $l_{\text{ct},0} = 15$  m are fixed across scenarios, and Fig. 11 reports the results. In Fig. 11(I), it is observed that, as can be expected,  $m_D$  has a much larger effect on  $-\dot{y}_H(t_{\text{ejt}})$  compared to  $m_{\text{MU},0}$ . Similar trends are observed in Fig. 11(II), except that  $-\dot{y}_{\text{CoM}}(t_{\text{ejt}})$  only increased to approximately 2.2 m/s at the maximum (i.e., approximately 20 times less than the maximum observed  $-\dot{y}_H(t_{\text{ejt}})$ ). It is interesting to note that  $-\dot{y}_{\text{CoM}}(t_{\text{ejt}})$  becomes negative for  $m_D >$  approximately 1.0 kg; this indicates that it is possible for the RESTORE system to gain velocity in the positive along-track direction as a product of the ejection maneuver. Fig. 11(III) examines the fuel consumed; as expected, lower debris mass and lower MU mass result in lower fuel consumed for the maneuver (and correspondingly, lower ejection time).

Next, we study the effects of varying the corner thread unstretched length  $l_{\text{ct},0}$  and the thrust magnitude  $F_T$ ; parameters  $m_D = 0.5$  kg,  $m_{\text{MU},0} = 3.5$  kg,  $\psi_0 = 15^\circ$ , and  $\phi = 75^\circ$  are fixed across scenarios. Fig. 12(I) shows that  $-\dot{y}_H(t_{\text{ejt}})$  increases proportionally with both parameters; however,  $F_T$  has a much greater effect on the quantity, which is to be expected as a result of the clear association between applied thrust and experienced acceleration (i.e., change in velocity) per Eq. (19). Similar trends to those of Fig. 12(I) are observed in Fig. 12(II-III), where  $-\dot{y}_{\text{CoM}}(t_{\text{ejt}})$  and total fuel consumed are maximum, at approximately 2.2 m/s and 0.11 kg, for  $l_{\text{ct},0} = 15.0$  m and  $F_T = 44$  N. In contrast, the effects of varying the corner thread length on the ejection time are minimal.

#### 4.3.2. Equilibrium analysis for the ejection dynamics using a rigid-arm model

In Section 4.3.1, situations were observed in which the debris is dragged by the RESTORE system in the Ejection Phase. This unintended behavior should be avoided and its cause investigated, as when it occurs, the fuel required for the maneuver increases significantly. The observations made for Fig. 10 indicate that for the specified initial net and thrust angles, the time derivatives of  $\psi$  are close to zero (i.e., the system is close to its equilibrium configuration); accordingly, an equilibrium analysis for the equations of motion is suitable to investigate the cause of this behavior. However, because of the discontinuous nature of the equations of motion in Eq. (19) – resulting from the tension dynamics defined by Eq. (4) – the three-DoF model is not suitable for such an analysis. With this limitation in mind, a further simplified model is derived and employed for the following equilibrium analysis, where – assuming that the arm-links are stiff and in tension during the ejection – each arm-link is approximated as a rigid, massless rod connecting either point  $P$  or  $Q$  to the central mass  $H$ . With these assumptions, the dynamics of the system can be fully described using two DoF (i.e., using  $y_H$  and  $\psi$  as the system's generalized coordinates), and its equations of motion can be determined using the Euler-Lagrange equations:

$$c \frac{d}{dt} \left( \frac{\partial L}{\partial \dot{y}_H} \right) - \frac{\partial L}{\partial y_H} = Q_{y_H} \quad (26a)$$

$$c \frac{d}{dt} \left( \frac{\partial L}{\partial \dot{\psi}} \right) - \frac{\partial L}{\partial \psi} = Q_\psi \quad (26b)$$

where  $L = 0.5m_H\dot{y}_H^2 + m_P(\dot{y}_H^2 + 2\dot{y}_H l_0\dot{\psi} \sin(\psi) + (l_0\dot{\psi})^2)$  is the Lagrangian of the two-DoF system, which is also equivalent to the kinetic energy of the system with respect to the  $C$  frame. The length of the rigid arm is defined as  $l_0 = 0.5L_{\text{side}} + l_{\text{ct},0}$ . The variable  $Q_{y_H} = \mathbf{F}_{T,P} \cdot \frac{\partial \mathbf{r}_{P/C}}{\partial y_H} = \mathbf{F}_{T,Q} \cdot \frac{\partial \mathbf{r}_{Q/C}}{\partial y_H}$  is the generalized force corresponding to the generalized coordinate  $y_H$ , while  $Q_\psi = \mathbf{F}_{T,P} \cdot \frac{\partial \mathbf{r}_{P/C}}{\partial \psi} = \mathbf{F}_{T,Q} \cdot \frac{\partial \mathbf{r}_{Q/C}}{\partial \psi}$  is the generalized force corresponding to the generalized coordinate  $\psi$ . Expanding the above equations and solving for  $\ddot{y}_H$  and  $\ddot{\psi}$  results in the following equations of motion:

$$\ddot{y}_H = -\frac{\beta_1 \sin(\psi) - \beta_2 l_0}{l_0(-2m_P \sin^2(\psi) + m_H + 2m_P)} \quad (27a)$$

$$\ddot{\psi} = \frac{\beta_1 m_H + 2\beta_2 m_P - 2\beta_2 l_0 m_P \sin(\psi)}{2m_P l_0^2 (-2m_P \sin^2(\psi) + m_H + 2m_P)} \quad (27b)$$

where  $\beta_1 = 2F_T l_0 (\sin \phi \cos \psi - \cos \phi \sin \psi)$  and  $\beta_2 = -2m_P l_0 \psi^2 \cos(\psi) - 2F_T \cos \phi$ . The two-DoF model and the three-DoF model were found to exhibit very similar dynamics overall; interested readers may refer to Appendix B for simulation results.

To perform the equilibrium analysis using the two-DoF model, the time derivatives of Eq. (27b) are set to zero<sup>6</sup>; the equation can then be

<sup>6</sup> Note that Eq. (27a), which describes the translational dynamics of the two-DoF system, is not considered for equilibrium analysis, since the focus here is to determine why the system's shape – as described by  $\psi$  – does not change over time in the outlier scenarios.

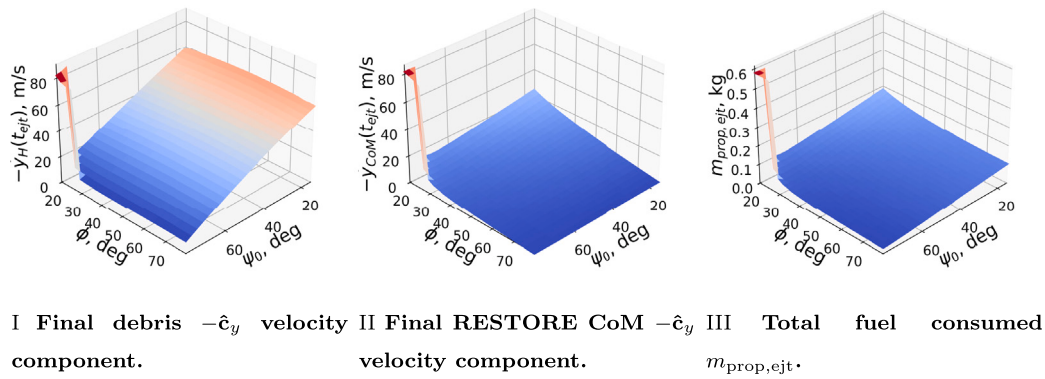


**Fig. 10.** Ejection phase dynamics quantities obtained by varying  $\psi_0$  and  $\phi$ . (For interpretation of the references to color in this figure legend, the reader is referred to the web version of this article.)

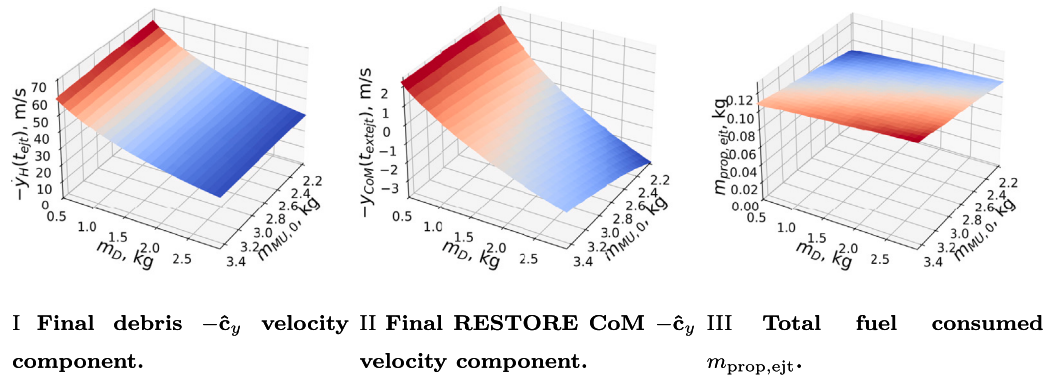


**Fig. 11.** Ejection phase dynamics quantities obtained by varying initial MU mass and debris mass.

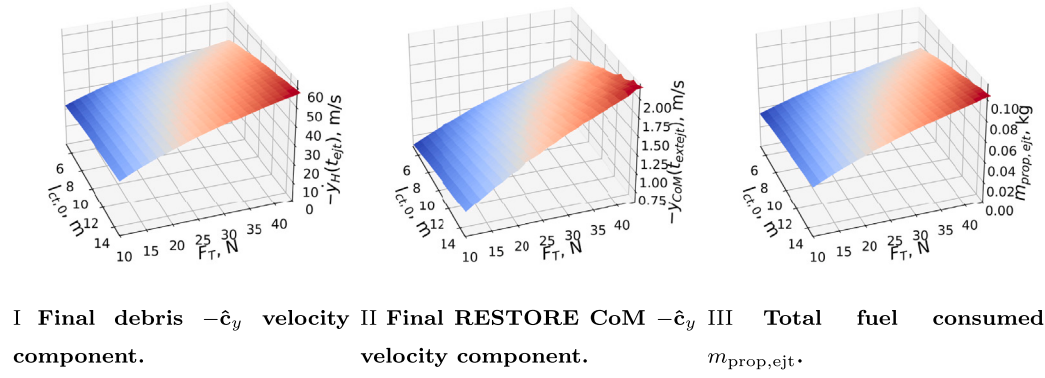


**Fig. 12.** Ejection phase dynamics quantities obtained by varying corner thread length and thrust magnitude.

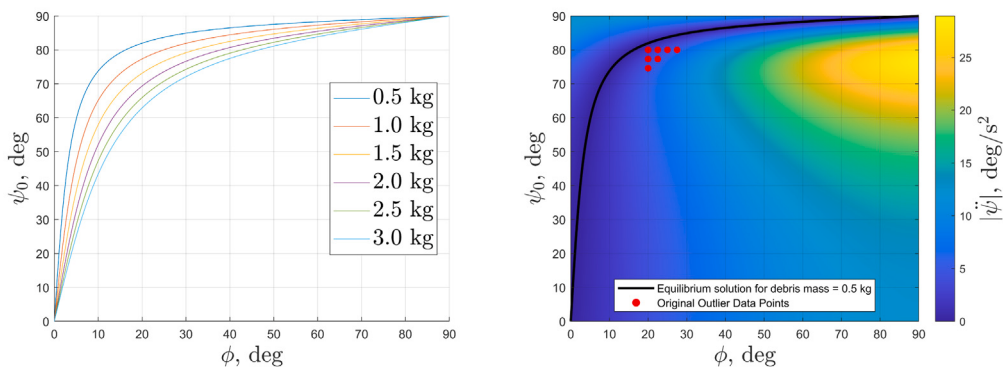
algebraically simplified to yield the following expression:

$$0 = m_H(\sin \phi \cos \psi - \cos \phi \sin \psi) + 2m_p \sin \phi \cos \psi \quad (28)$$

The expression is observed to depend on  $m_p$ ,  $m_H$ ,  $\psi$ , and  $\phi$ , indicating that the model's equilibrium solution depends on the employed mass properties, as well as its initial geometry and the direction of the applied control force.

To acquire insights into how changing system parameters affect the equilibrium solution for the two-DoF model, the values of Eq. (28) are plotted in Fig. 13 using varying  $m_H$ ,  $\psi$ , and  $\phi$  values, with  $m_p$  fixed to 7.27 kg as was done to obtain the results of Fig. 10. A family of equilibrium solutions for varying  $\psi_0$  and  $\phi$  is shown in Fig. 13(I) for debris masses varying between 0.5 kg and 3.0 kg. It can be seen that, for any given  $\phi$  value, the corresponding  $\psi_0$  for the displayed curves

are smaller for greater debris mass; for example, with  $\phi = 20^\circ$ , the equilibrium solution corresponds to  $\psi_0 = 82^\circ$  and  $\psi_0 = 62.9^\circ$  for the 0.5 kg and 3.0 kg debris, respectively. For the 0.5 kg debris case, Fig. 13(II) provides a heat map of  $|\dot{\psi}|$  at  $t = 0$ , constructed using Eq. (27b), together with the corresponding equilibrium solutions. The outlier data points from the discontinuous region of Fig. 10 are also marked as red dots, and are found to be in the dark-blue band in the neighboring region of the equilibrium solution curve, where the initial acceleration magnitude is small (i.e., below approx.  $5.5^\circ/\text{s}^2$ ). These results confirm that  $\psi_0$  and  $\phi$  only need to be close to the equilibrium solution for  $\dot{\psi}$  to be small enough such that the dragging phenomenon is observed. Nonetheless, it should be noted that, according to the conclusions of Section 4.3.1, the RESTORE system should ideally employ parameters that are far from those of outlier data points (e.g.,  $\phi = 75^\circ$  and  $\psi_0 = 15^\circ$ )



I Solutions for  $\dot{\psi} = 0$  for varying debris mass. II Heat map of  $|\dot{\psi}|$  at  $t = 0$  for 0.5 kg debris.

Fig. 13. Plots for the equilibrium analysis of  $\dot{\psi}$  for Phase IV.

for optimal overall ejection performance; therefore, the unintended dragging phenomenon is unlikely to occur for the system in actual ADR missions.

#### 4.3.3. Results of ejection simulations performed using the high-fidelity model

Using the preferred system design and control parameters found from the study of the planar simplified model, we are now in a position to use the high-fidelity model to compute the tension the RESTORE system experiences throughout the ejection maneuver and determine whether any thread breakage will occur. Debris masses of both  $m_D = 0.5$  kg and  $m_D = 3.0$  kg are considered for this analysis. The high-fidelity system possesses a geometric configuration described by  $\psi_0 = 15^\circ$ , with the ejection performed using control parameters  $F_T = 22$  N and  $\phi = 75^\circ$ . For  $m_D = 0.5$  kg, maximum tensions of 273 N and 427 N, respectively, were experienced by the net and the corner threads at the conclusion of the maneuver (i.e., when the debris is released from the net) at approximately 2.6 s. With  $m_D = 3.0$  kg, the net proper and corner threads achieved lower maximum tensions, of 114 N and 74 N respectively, also at the conclusion of the maneuver at approximately 2.8 s. The lower maximum tensions experienced with  $m_D = 3.0$  kg are explained by the decreased acceleration experienced by the system as a result of the same applied thrust. Considering that the ultimate tensile strength of Technora is approximately  $\sigma_{\max} = 3350$  MPa [50], the maximum allowable thread tensions are computed as:

$$T_{\text{net,max}} = \beta \sigma_{\max} \pi r_{\text{net}}^2 = 901.1 \text{ N} \quad (29a)$$

$$T_{\text{ct,max}} = \beta \sigma_{\max} \pi r_{\text{ct}}^2 = 3604.6 \text{ N} \quad (29b)$$

where the coefficient  $\beta = 0.3425$  quantifies how packed the fibers strands are in each thread [32]. The maximum tension experienced by the corner threads and net proper in the two cases are observed to be between approximately 8% and 30% of the tensile limits, signifying that the RESTORE system can withstand the ejection maneuver for small-medium sized debris.

It should be noted that, in the high-fidelity simulation with  $m_D = 0.5$  kg,  $-\dot{y}_H(t_{\text{ejt}})$  was changed by 63.2 m/s throughout the ejection. With the planar simplified model of Section 3.4 (i.e., the three-DoF model),  $-\dot{y}_H(t_{\text{ejt}})$  was changed by 61.0 m/s, which is very similar. However, in the high-fidelity and simplified model simulations with  $m_D = 3.0$  kg,  $-\dot{y}_H(t_{\text{ejt}})$  was changed by 28.2 and 32.3 m/s, respectively; this larger difference suggests that the simplified model is less accurate when a larger debris mass is used. More in-depth ejection dynamics comparison between the simplified and high-fidelity net models will be a subject of future research.

#### 5. Comparison of deorbiting scenarios

With the models analyzed and validated, we now proceed to quantitatively assess the performance of the RESTORE system in several ADR scenarios of interest. As in Section 4, the initial mass of the RESTORE system is assumed to be  $m_{\text{sys},0} = 14.54$  kg. We consider two ADR missions requiring the removal of 5 debris objects with  $m_D = 3.0$  kg and  $m_D = 0.5$  kg, respectively. The debris objects are assumed to be clustered relatively close together with orbit altitudes of {782, 781, 780, 779, 778} km and true anomaly offsets of  $5^\circ$  between debris.

In both scenarios, the mass of the RESTORE system decreases after each mission phase<sup>7</sup> in accordance with the fuel consumption formulations presented in Section 3. In Phase I, the required  $\Delta v_{\text{rnd},i}$  for each debris includes contributions from Close Rendezvous and Final Approach stages (as described in Section 3.1) with the maneuver times (assumed to be the same for all 5 deorbiting events) of  $t_{\text{rnd},i} = 3200$  s and  $t_{\text{rnd},i} = 1600$  s, respectively. At the end of the Close Rendezvous stage, the system is set to have the same orbital velocity as the debris (i.e.,  $v_{f,\text{rnd}} = 0$ ). The final system speed relative to the debris at the end of the Final Approach stage is selected to be  $v_{f,\text{rnd}} = 0.2$  m/s, based on the analysis of Section 4.1. In Phase II, due to the high computational cost of the full-net simulations, the total fuel consumptions are assumed to be 0.052 and 0.04 kg for  $m_D = 3.0$  kg and  $m_D = 0.5$  kg, respectively, based on the performed sample simulations. The  $\Delta v_{\text{env},i}$  costs for  $m_D = 3.0$  kg and  $m_D = 0.5$  kg were similarly assumed as 3.3 and 2.7 m/s, respectively.

To deorbit each debris (via the maneuvers of Phases III–IV), the RESTORE system changes its orbital speed by only  $\Delta v_{\text{drag}}$ , as it was demonstrated that the RESTORE system's CoM speed is minimally altered (<2.2 m/s) throughout the ejection maneuver (see Fig. 11(II)). To achieve the deorbiting goal of modifying the circular orbit of each debris (with approximately 780 km orbit altitude) to an elliptical orbit with a targeted perigee altitude of  $h_{\text{deo}} = 275$  km, approximately  $\Delta v_{\text{deo}} = 138$  m/s is required. Through the ejection maneuver, the RESTORE system can impart speed changes of approximately 30 and 62 m/s for  $m_D = 3.0$  kg and  $m_D = 0.5$  kg, respectively (see Fig. 11); therefore,  $p_{\text{drag}}$  is set to be equal to  $100(1 - 30/\Delta v_{\text{deo}}) = 78\%$  and  $100(1 - 62/\Delta v_{\text{deo}}) = 55\%$  for  $m_D = 3.0$  kg and  $m_D = 0.5$  kg, respectively. The developed models and control algorithm for Phase IV ignored the stabilization of the RESTORE system after the ejection maneuver; accordingly, the fuel cost required for Phase IV – computed via Eq. (20)

<sup>7</sup> For the numerical simulations of Phases I, II, and IV, the initial mass of each MU,  $m_{\text{MU},0}$ , is approximated to be equal to the average mass of all 4 MUs at the end of the previous mission phase.

**Table 2**

Mission quantities of ADR scenario with  $p_{\text{drag}} = 78\%$ ,  $m_{\text{sys},0} = 14.54 \text{ kg}$ ,  $m_D = 3.0 \text{ kg}$ .

Quantities	Debris 1	Debris 2	Debris 3	Debris 4	Debris 5
$t_{\text{tot},i}$ , h	18.091	18.088	18.084	18.081	1.37
$\Delta v_{\text{rnd},i}$ , km/s	0.003	0.003	0.003	0.003	0.003
$\Delta v_{\text{env},i}$ , km/s	0.003	0.003	0.003	0.003	0.003
$\Delta v_{\text{drag},i}$ , km/s	0.107	0.107	0.107	0.107	0.107
$\Delta v_{\text{reco},i}$ , km/s	0.109	0.109	0.109	0.109	0
$\Delta v_{p,i}$ , km/s	0.007	0.007	0.007	0.007	0
$\Delta v_{\text{tot},i}$ , km/s	0.230	0.230	0.229	0.229	0.113
$m_{\text{final},i}$ , kg	12.886	11.350	10.055	8.847	8.167
Total quantity					
$\Delta v_{\text{tot}} = \sum_{i=1}^5 \Delta v_{\text{tot},i}$ , km/s	1.034				
$(m_{\text{sys},0} - m_{\text{final}})/4$ , kg	1.593				

**Table 3**

Mission quantities of ADR scenario with  $p_{\text{drag}} = 55\%$ ,  $m_{\text{sys},0} = 14.54 \text{ kg}$ ,  $m_D = 0.5 \text{ kg}$ .

Quantities	Debris 1	Debris 2	Debris 3	Debris 4	Debris 5
$t_{\text{tot},i}$ , h	18.101	18.097	18.094	18.090	1.37
$\Delta v_{\text{rnd},i}$ , km/s	0.003	0.003	0.003	0.003	0.003
$\Delta v_{\text{env},i}$ , km/s	0.003	0.003	0.003	0.003	0.003
$\Delta v_{\text{drag},i}$ , km/s	0.076	0.075	0.075	0.075	0.075
$\Delta v_{\text{reco},i}$ , km/s	0.077	0.077	0.077	0.077	0
$\Delta v_{p,i}$ , km/s	0.007	0.007	0.007	0.007	0
$\Delta v_{\text{tot},i}$ , km/s	0.166	0.166	0.166	0.166	0.084
$m_{\text{final},i}$ , kg	13.39	12.331	11.347	10.436	9.955
Total quantity					
$\Delta v_{\text{tot}} = \sum_{i=1}^5 \Delta v_{\text{tot},i}$ , km/s	0.745				
$(m_{\text{sys},0} - m_{\text{final}})/4$ , kg	1.146				

– is multiplied by 1.5 (as a heuristic estimate) to approximate the fuel needed for stabilization. Quantities regarding Phase V of the mission (i.e.,  $\Delta v_{\text{reco},i}$  and  $\Delta v_{p,i}$ ) are computed via analytical classical orbital expressions as described in Section 3.5 under the assumption that the spacecraft performs  $k = 10$  phasing orbits to meet-up with each debris. It is noted that Phase V is not performed after the ejection of the last debris, as the RESTORE system has already completed its mission at that point.

Tables 2 and 3 display ADR mission quantities – including total time,  $\Delta v$  costs, and total fuel consumption – for the removal of 5 debris objects with  $m_D = 3.0 \text{ kg}$  and  $m_D = 0.5 \text{ kg}$ , respectively. The increased  $p_{\text{drag}}$  – required due to the reduced acceleration that can be imparted onto the heavier debris during the ejection maneuver – affected both the relocation and deorbiting maneuvers costs. With  $m_D = 3.0 \text{ kg}$  and  $m_D = 0.5 \text{ kg}$ , the costs  $\Delta v_{\text{reco},i}$  and  $\Delta v_{\text{drag},i}$  are close to 77 m/s and 76 m/s and to 109 m/s and 107 m/s, respectively. As expected from the  $\Delta v$  cost differences, the RESTORE system consumed much less fuel (1.146 kg/MU) when it was tasked with deorbiting debris with  $m_D = 0.5 \text{ kg}$  in comparison to debris with  $m_D = 3.0 \text{ kg}$  (requiring 1.593 kg/MU). In Section 6, it will later be shown that such an amount of fuel can be carried by MUs constructed using commercial off-the-shelf components with flight heritage.

The effects of varying additional mission parameters on the overall mission cost are examined in Table 4 for six unique scenarios. Unless listed otherwise, the  $\Delta v_{\text{tot}}$  and  $(m_{\text{sys},0} - m_{\text{final}})/4$  values are computed using the same methods and assumed parameters as for the construction of Tables 2 and 3. Case 1 is the most challenging scenario, with 3-kg debris, larger orbit altitude separation ( $R_{D,i} - R_{D,i-1}$ ), and larger true anomaly spacings  $\theta_{\text{offset}}$  between different debris. Comparatively, Case 4 presents the least challenging scenario, where the debris objects are of lower mass and closer together. The debris orbit altitudes are {790, 785, 780, 775, 770} km in Cases 1–2, and {782, 781, 780, 779, 778} km for all other cases. It should be noted that Cases 3–4 are the same as those examined in detail in Tables 2 and 3, respectively. The analyses

**Table 4**

Case studies for varying deorbiting mission parameters.

Case	$R_{D,i} - R_{D,i-1}$ , km	$m_D$ , kg	$\theta_{\text{offset}}$ , °	$p_{\text{drag}}$ , %	$\Delta v_{\text{tot}}$ , km/s	$(m_{\text{sys},0} - m_{\text{final}})/4$ , kg
1	5	3	72	78	1.438	1.949
2	5	3	5	78	1.059	1.618
3	1	3	5	78	1.034	1.593
4	1	0.5	5	55	0.745	1.146
5	1	3	5	63	0.897	1.437
6	1	0.5	5	32.5	0.466	0.804

in Table 4 also consider hypothetical scenarios in Cases 5–6, where it is hypothesized that more effective ejection control can be developed in the future to enable increased debris ejection speeds, resulting in the reduction of  $p_{\text{drag}}$  values to 63% and 32.5% for  $m_D = 3.0 \text{ kg}$  and  $m_D = 0.5 \text{ kg}$ , respectively.

In Table 4, it can be seen with Case 1 that as much as 1.949 kg of fuel per MU (i.e., 7.8 kg for the entire RESTORE system) is needed to deorbit 5 debris objects with  $m_D = 3 \text{ kg}$ . It is observed that choosing debris objects with small true anomaly offsets from one another (such as in Case 2) notably reduces the required  $\Delta v_{\text{tot}}$  as a product of smaller phasing burns. Comparing Cases 2 and 3 it can be concluded that selecting a debris cluster with lower orbit altitude separation has a relatively small effect on the overall mission costs. Instead, the mission cost is notably reduced for lower debris mass (see Case 4). Finally, Cases 5 and 6 demonstrate that increasing the deorbiting  $\Delta v$  contribution of the ejection maneuver (i.e., lowering  $p_{\text{drag}}$ ) can notably reduce mission costs as expected. As an example, only 0.804 kg/MU of fuel is needed in Case 6 compared to 1.146 kg/MU in Case 4.

## 6. Systems engineering

It is natural to ask whether the MUs proposed in this effort can be realized with existing high-TRL technology. Accordingly, in the following analysis, we briefly study the systems engineering aspect of RESTORE, i.e., the envisioned subsystems required for each MU. First – although it was neglected for the modeling and simulation analyses within this work – each MU must have an ADCS to perform pose estimation and appropriately orient the RESTORE system through the mission. To provide the required thrust for maneuvering throughout the ADR mission, a chemical rocket propulsion system is required. Each MU is also equipped with a GPS receiver for far-range navigation and with a monocular camera to allow for visual debris inspection and close-range navigation. To store and process telecommand data from mission control and compute the appropriate thrust control inputs, each MU requires a command and data handling (CDH) computer. For communication, transceivers and antennas must also be present to uplink and downlink to and from the RESTORE system. Each MU is equipped with a battery, integrated power board, and solar panels to store and generate electrical power. Lastly, as is typical for small spacecraft, thermal control of each MU is performed passively via insulation layers [33].

Table 5 proposes a strawman design for a MU that uses existing, commercially available subsystems. The table lists the subsystem component masses for each MU, as well as the combined total mass. Most of the component mass values were obtained from Ref. [33], which details the state-of-the-art technologies currently in-use with small spacecraft. It should be noted that all of the named subsystem components in Table 5 have flight heritage with flown nanosatellites and microsatellites. The system mass limit for each MU is 3.5 kg, as used in the analyses of this work. The MU frame structure mass was set to 0.300 kg to account for the 2U frame mass as per Ref. [51] (0.206 kg) plus fairings, passive thermal control systems, as well as possible structural reinforcements needed to attach the net (0.094 kg, i.e., approximately 50% of the frame mass). The mass budget for the harnessing equipment was based on

**Table 5**  
System components and mass.

S/C component	Component name	Total mass, g
<b>S/C structural components</b>		
2U structure [53]	2-Unit CubeSat Structure	300
Solar panels [54]	ISIS Small satellite solar panels	100
Harnessing [52]	–	120
<b>GNC</b>		
Camera [55]	NanoCam C1U	169
GPS receiver [33]	piNAV-NG	24
GPS antennae [33]	piPATCH-L1E1	50
Integrated ADCS [33]	IADCS-100	400
<b>Electrical</b>		
Battery and power board [56]	Compact Electrical Power System 2(A)	189
<b>Computing hardware</b>		
On-Board computer [57]	ISIS On Board Computer	100
<b>Communication</b>		
Transceiver [33]	NANOcomm-2	110
Antennae [33]	NanoCom ANT430	30
<b>Propulsion</b>		
Thruster [48]	MR-106L 22N	590
System miscellaneous	(see text)	100
Fuel	–	1218

the component mass budget allocated for the flown qbee50-LTU-OC 2U Cubesat [52].

A mass budget of 0.100 kg is also included to account for miscellaneous propulsion system components other than the engine itself (e.g., the propellant storage tank, and engine microcontroller). Therefore, to comply with the mass limit of 3.5 kg, the maximum amount of fuel allowed is 1.218 kg. It is noted that, according to the debris removal missions presented in Tables 2 and 3, three pieces of 3-kg debris – using  $(m_{sys,0} - m_{final,3})/4 = 1.121$  kg/MU of fuel – or five pieces of 0.5-kg debris – using  $(m_{sys,0} - m_{final,5})/4 = 1.146$  kg/MU of fuel – can be removed from orbit within the available fuel budget.

We also assess the MU's power consumption. Based on the required subsystem components of each MU, Table 6 lists the power consumption of the electrical components and the duty cycle percentages  $d_1$  and  $d_2$  assigned for different power consumption modes. The first duty cycle  $d_1$  is allocated when the RESTORE system is in *coasting mode* – to travel between debris – in Phases I and V. For this power mode, the system minimally activates the control of the main engines and ADCS to maneuver the spacecraft to the desired orbits and orient the spacecraft's solar panels towards the sun for electrical power generation. Note that in this work, as a first-order approximation, the electrical power required to operate the engine microcontroller is assumed to be equal to the amount required to operate the ADCS system. The main thrusters themselves also require some electrical power for valve actuation and component heating. Most of the downlink of the system's status information and the uplink of the telecommand data are set to happen during the coasting mode as well. In this mode, the on-board camera is not needed as the spacecraft's GPS system performs the navigation. The duty cycles assigned for the transceiver and GPS receiver in this power mode are set to be similar to those of Ref. [58], which examined the systems engineering of an 8U Cubesat-sized spacecraft designed for debris deorbiting. With the planned subsystem duty cycle allocations, the power consumption is approximately 11 W; this is similar to the power consumption observed with similar-sized flown Cubesats [59,60].

From the instance when the RESTORE system comes into close proximity with each debris until the end of the ejection (i.e., Phases II–IV), the *active control mode* is activated, with duty cycle  $d_2$ . In this mode, both the main propulsion and ADCS control systems are set to high activity. The on-board camera is also set to be active – except for during the dragging phase where the debris is trapped inside the

system – to observe the debris's state and allow the system to perform relative navigation with it. As the RESTORE system is envisioned to perform debris removal maneuvers autonomously with minimal inputs from ground stations, uplinking and downlinking of data during Phases II–IV are kept to a minimum. With these planned subsystem duty cycle allocations, the power consumption is approximately 31 W, significantly higher than in the coasting mode, but still capable of being supplied by the chosen “Compact Electrical Power System 2(A)” spacecraft component [33,56].

## 7. Conclusion

This work proposed the RESTORE system and the corresponding mission concept to address the growing demand for ADR solutions. The RESTORE system combines the advantages of contactless debris removal methods (i.e., the reusability and robustness to uncertainties in the debris states) with the advantages of contact-based removal methods (i.e., high control authority). To demonstrate the feasibility of the concept for removing small-to-medium sized debris, we performed a preliminary design analysis of the system and assessed its performance in relevant LEO ADR scenarios.

This study first provided an overview of the system and mission concept. Then, models for the system were presented to explore the dynamics and fuel-cost estimates for the various phases of the ADR mission. In particular, we used numerical models to study the Close Rendezvous and Final Approach, Envelopment, and Ejection phases. The RESTORE system could successfully perform maneuvers to approach and capture debris using a reference-path tracking PD controller. The RESTORE system could also safely perform the slingshot ejection maneuver, imparting a significant change to the debris's orbital speed while incurring only a minor change to the system's orbital speed. The systems engineering of the concept indicated that the construction and deployment of the RESTORE system are feasible with present technology.

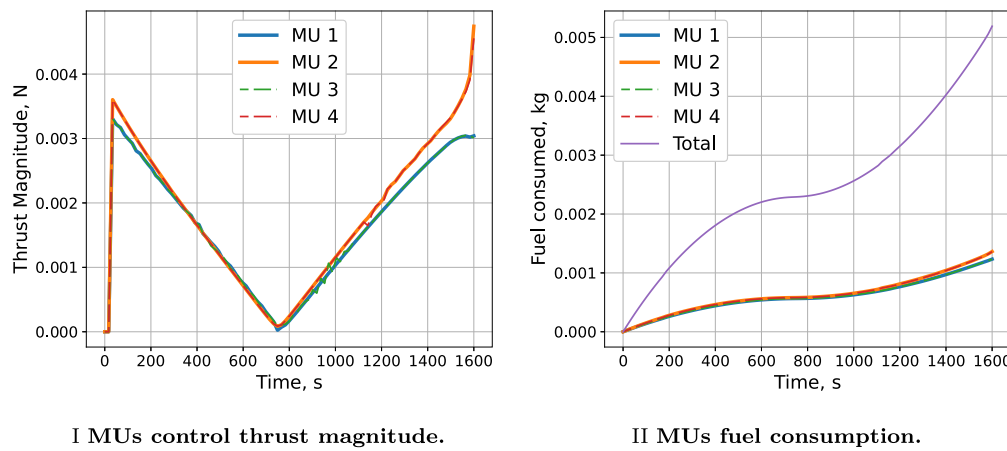
Additional research must be done to further demonstrate and analyze the capabilities of the RESTORE system. Perturbation forces, such as (but not limited to) residual atmospheric drag and non-spherical gravitational potential, will be the focus of future simulations to study the system's dynamical behavior within a more realistic environment. Algorithms for state estimation must also be developed for the system to conduct robust navigation throughout the ADR mission. To enable the system to handle uncertainties in the state estimation, robust or adaptive thrust control techniques should also be formulated for the different phases of the mission. Safety constraints will also be considered in future work for the control design process, thus ensuring that the MUs do not collide with each other or the debris. More research is also needed to analyze strategies for mitigating entanglement risks of debris with the mesh of the net (e.g., using low-friction coating substances on the threads, determining preferred net mesh sizes, or using a membrane in place of a net). The possibility of performing in-orbit refueling of the RESTORE system by another spacecraft after the last debris has been deorbited should be explored as well.

## CRediT authorship contribution statement

**Achira Boonrath:** Writing – original draft, Visualization, Software, Methodology, Formal analysis, Conceptualization. **Federico Rossi:** Writing – review & editing, Supervision, Resources, Methodology, Funding acquisition, Conceptualization. **Issa A. Nesnas:** Writing – review & editing, Supervision, Resources, Methodology, Conceptualization. **Eleonora M. Botta:** Writing – review & editing, Supervision, Software, Resources, Project administration, Methodology, Formal analysis, Conceptualization.

**Table 6**  
System components and power consumption.

S/C component	Component name	Power, mW	$d_1$ , %	$d_2$ , %
<b>GNC</b>				
Camera	NanoCam C1U	1300	0	75
GPS receiver	piNAV-NG	124	50	50
Integrated ADCS	IADCS-100	2700	10	100
<b>Computing hardware</b>				
On-board computer	ISIS On Board Computer	550	100	100
<b>Communication</b>				
Transceiver	NANOcomm-2	5000	40	10
<b>Propulsion</b>				
Engine controller*	–	2700	10	75
Engine valve actuator	MR-106L 22N	25100	10	75
Engine components heater	MR-106L 22N	10060	50	50
<b>Total quantities</b>				
Total power	–	–	≈11 000 mW	≈31 000 mW



I MUs control thrust magnitude.

II MUs fuel consumption.

Fig. A.1. Additional plots concerning the final approach maneuver.

#### Declaration of competing interest

The authors declare that they have no known competing financial interests or personal relationships that could have appeared to influence the work reported in this paper.

#### Acknowledgments

The authors express gratitude toward CM Labs Simulations for providing licenses for the Vortex Studio simulation framework. During the preparation of this work the authors used Grammarly in order to correct accidental syntax and grammar mistakes during the writing process. After using this tool/service, the authors reviewed and edited the content as needed and take full responsibility for the content of the publication.

#### Appendix A. Additional results for the analysis of phase I

Fig. A.1(I) displays the magnitude of the thrust forces commanded by the PD controller in the Final Approach maneuver; the thrusts applied on the MUs are minimal compared to the maximum available thrust magnitude, of 22 N. It should be noted that this small-magnitude (compared to the saturation limit) thrust profile could be achieved via the pulse-width modulation of each thruster, though further research must be done to verify the control approach when it is applied onto a physical thruster. Fig. A.1(II) displays the fuel consumption by the MUs for the maneuver. All MUs each consume less than 1.3 g of fuel, with the combined system only using approximately 5.1 g of fuel.

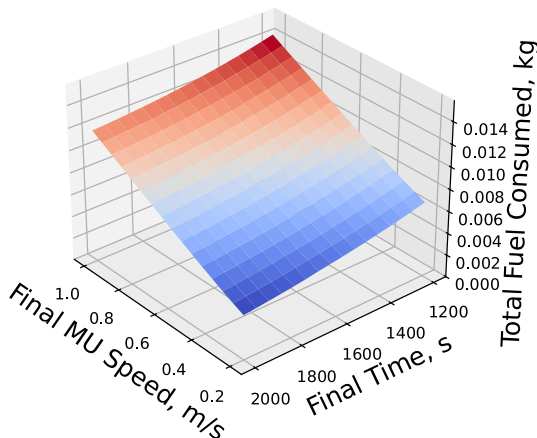
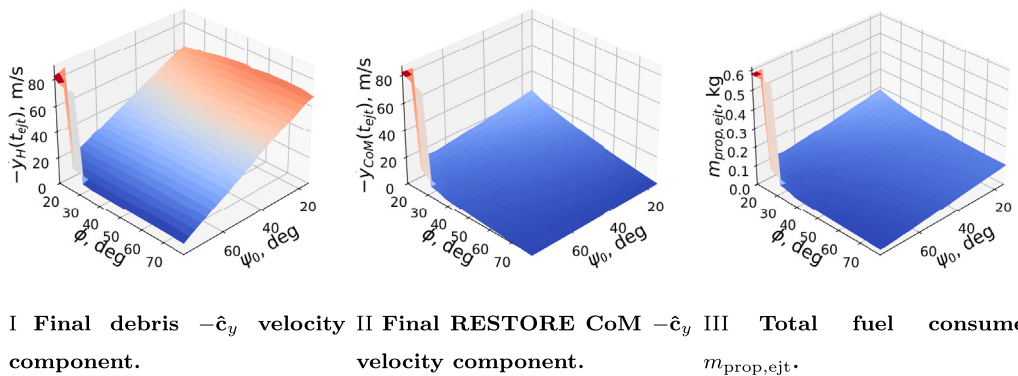


Fig. A.2. Total fuel consumed for the final approach maneuver as a function of  $t_{f,rd}$  and  $v_{f,rd}$ .

#### Funding sources

Achira Boonrath acknowledges the University at Buffalo Presidential Fellowship. Part of this research was carried out at the Jet Propulsion Laboratory, California Institute of Technology, under a contract with the National Aeronautics and Space Administration, United States (80NM0018D0004).



**Fig. B.1.** Ejection phase dynamics quantities obtained by varying  $\psi_0$  and  $\phi$  for the rigid arm-links model.

**Fig. A.2** displays the total fuel consumption as a function of the final time  $t_{\text{rnd}}$  and the desired final speed for each MU  $v_{f,\text{rnd}}$ . The total fuel consumption increases for lower  $t_{\text{rnd}}$  and higher  $v_{f,\text{rnd}}$ , though it is clear that  $v_{f,\text{rnd}}$  has a larger effect. This finding indicates that more flexibility is allowed for selecting the desired maneuver time compared to the final approach speed (which has to be kept relatively low).

## Appendix B. Comparison of 2-DoF and 3-DoF models for phase IV

The dynamical similarity between the three-DoF and the two-DoF models must be verified to ensure that the latter can be used as a substitute for the former in the equilibrium analysis of Section 4.3.2. For the verification, the results of Fig. 10 are reproduced and shown in Fig. B.1 using the two-DoF model. It can be appreciated that the simulation results for the two models are very similar across the varying initial  $\psi_0$  and  $\phi$  angles employed, with both sets of results exhibiting discontinuities for large  $\psi_0$  and small  $\phi$  values. Outside the discontinuous region, the values for  $-\dot{y}_H(t_{\text{ejt}})$  and  $-\dot{y}_{\text{CoM}}(t_{\text{ejt}})$  are found to be similar between the two models, although they are slightly higher with the two-DoF model than with the three-DoF model (see Figs. 10(I-II) and B.1(I-II)). For example, with  $\phi = 80^\circ$  and  $\psi_0 = 15^\circ$ ,  $-\dot{y}_H(t_{\text{ejt}})$  is approx. 60.2 m/s and 67.7 m/s for the three- and two-DoF models, respectively. Meanwhile, the values for  $m_{\text{prop},\text{ejt}}$  are indistinguishable between the two models (see Figs. 10(III) and B.1(III)). The authors also replicated the results of Figs. 11 and 12 using the two-DoF model; they are omitted, for brevity, as they were found to be very similar between the models.

## References

- [1] J. Liou, Risks from orbital debris and space situational awareness, in: IAA Conference on Space Situational Awareness, ICSSA, Vol. JSC-E-DAA-TN76975, 2020.
- [2] P. Anz-Meador, J.-C. Liou, Analysis and consequences of the iridium 33-cosmos 2251 collision, in: 38th COSPAR Scientific Assembly, Bremen, Germany, July 2010.
- [3] A. Ledkov, V. Aslanov, Review of contact and contactless active space debris removal approaches, Prog. Aerosp. Sci. 134 (2022) 100858, <http://dx.doi.org/10.1016/j.paerosci.2022.100858>.
- [4] M. Shan, J. Guo, E. Gill, A review and comparison of active space debris capturing and removal methods, Prog. Aerosp. Sci. 80 (2015) 18–32, <http://dx.doi.org/10.1016/j.paerosci.2015.11.001>.
- [5] E.M. Botta, I. Sharf, A. Misra, Evaluation of net capture of space debris in multiple mission scenarios, in: 26th AAS/AIAA Space Flight Mechanics Meeting, AAS, Napa, California, February 2016.
- [6] E.M. Botta, I. Sharf, A.K. Misra, Simulation of tether-nets for capture of space debris and small asteroids, Acta Astronaut. 155 (2019) 448–461, <http://dx.doi.org/10.1016/j.actaastro.2018.07.046>.
- [7] M. Shan, J. Guo, E. Gill, Contact dynamic models of space debris capturing using a net, Acta Astronaut. 158 (2019) 198–205, <http://dx.doi.org/10.1016/j.actaastro.2017.12.009>.
- [8] R. Benvenuto, S. Salvi, M. Lavagna, Dynamics analysis and GNC design of flexible systems for space debris active removal, Acta Astronaut. 110 (2015) 247–265, <http://dx.doi.org/10.1016/j.actaastro.2015.01.014>.
- [9] P. Huang, F. Zhang, J. Ma, Z. Meng, Z. Liu, Dynamics and configuration control of the maneuvering-net space robot system, Adv. Space Res. 55 (4) (2015) 1004–1014, <http://dx.doi.org/10.1016/j.asr.2014.11.009>.
- [10] W. Zhu, Z. Pang, J. Si, G. Gao, Dynamics and configuration control of the tethered space net robot under a collision with high-speed debris, Adv. Space Res. 70 (5) (2022) 1351–1361, <http://dx.doi.org/10.1016/j.asr.2022.06.019>.
- [11] W. Zhu, Z. Pang, Z. Du, G. Gao, Z.H. Zhu, Multi-debris capture by tethered space net robot via redeployment and assembly, J. Guid. Control Dyn. (2024) 1–18, <http://dx.doi.org/10.2514/1.G007908>.
- [12] F. Zhang, P. Huang, Z. Meng, Y. Zhang, Z. Liu, Dynamics analysis and controller design for maneuverable tethered space net robot, J. Guid. Control Dyn. 40 (11) (2017) 2828–2843, <http://dx.doi.org/10.2514/1.G002656>.
- [13] Y. Liu, P. Huang, F. Zhang, Y. Zhao, Robust distributed consensus for deployment of tethered space net robot, Aerosp. Sci. Technol. 77 (2018) 524–533, <http://dx.doi.org/10.1016/j.ast.2018.04.005>.
- [14] F. Zhang, P. Huang, Stability control of a flexible maneuverable tethered space net robot, Acta Astronaut. 145 (2018) 385–395, <http://dx.doi.org/10.1016/j.actaastro.2018.02.007>.
- [15] Y. Zhao, F. Zhang, P. Huang, Dynamic closing point determination for space debris capturing via tethered space net robot, IEEE Trans. Aerosp. Electron. Syst. 58 (5) (2022) 1, <http://dx.doi.org/10.1109/TAES.2022.3159626>.
- [16] A. Boonrath, F. Liu, E.M. Botta, S. Chowdhury, Learning-aided control of robotic tether-net with maneuverable nodes to capture large space debris, in: 2024 IEEE International Conference on Robotics and Automation, ICRA, IEEE, 2024, pp. 11737–11743, <http://dx.doi.org/10.1109/ICRA57147.2024.10610721>.
- [17] F. Liu, A. Boonrath, P. KrishnnaKumar, E.M. Botta, S. Chowdhury, Learning constrained corner node trajectories of a tether net system for space debris capture, in: AIAA AVIATION 2023 Forum, 2023, p. 3920, <http://dx.doi.org/10.2514/6.2023-3920>.
- [18] A.C. Boley, M. Byers, Satellite mega-constellations create risks in low earth orbit, the atmosphere and on earth, Sci. Rep. 11 (1) (2021) 1–8, <http://dx.doi.org/10.1038/s41598-021-89909-7>.
- [19] A. Ruggiero, P. Pergola, M. Andrenucci, Small electric propulsion platform for active space debris removal, IEEE Trans. Plasma Sci. 43 (12) (2015) 4200–4209, <http://dx.doi.org/10.1109/TPS.2015.2491649>.
- [20] T.S. Kelso, Celestrak, 2017, [Online]. Available: <https://celestrak.org/>. (Last Accessed 29 April 2025).
- [21] United States Space Command, Space-track,, 2017, [Online]. Available: <https://www.space-track.org/>. (Last accessed 29 April 2025).
- [22] A. Rossi, N. Sánchez-Ortiz, E. David, R. Oromolla, D. Grishko, Future activities in the near-earth space in the face of ever-increasing space traffic, Acta Astronaut. (2024) <http://dx.doi.org/10.1016/j.actaastro.2024.09.063>.
- [23] W.J. Faccenda, GEODSS: past and future improvements, MITRE Corp. (2000).
- [24] C. Pardini, W.K. Tobiska, L. Anselmo, Analysis of the orbital decay of spherical satellites using different solar flux proxies and atmospheric density models, Adv. Space Res. 37 (2) (2006) 392–400, <http://dx.doi.org/10.1016/j.asr.2004.10.009>.
- [25] H. Hakima, M.R. Emami, Deorbiter CubeSat mission design, Adv. Space Res. 67 (7) (2021) 2151–2171, <http://dx.doi.org/10.1016/j.asr.2021.01.005>.
- [26] A. Boonrath, E.M. Botta, Validation of models for net deployment and capture simulation with experimental data, J. Spacecr. Rockets (2023) 1–19, <http://dx.doi.org/10.2514/1.A35798>.

- [27] W. Huang, D. He, Y. Li, D. Zhang, H. Zou, H. Liu, W. Yang, L. Qin, Q. Fei, Nonlinear dynamic modeling of a tether-net system for space debris capture, *Nonlinear Dynam.* 110 (3) (2022) 2297–2315, <http://dx.doi.org/10.1007/s11071-022-07718-7>.
- [28] Y. Hou, C. Liu, H. Hu, W. Yang, J. Shi, Dynamic computation of a tether-net system capturing a space target via discrete elastic rods and an energy-conserving integrator, *Acta Astronaut.* 186 (2021) 118–134, <http://dx.doi.org/10.1016/j.actaastro.2021.05.029>.
- [29] G. Zhang, Q. Zhang, Z. Feng, Q. Chen, T. Yang, A simplified model for fast analysis of the deployment dynamics of tethered-net in space, *Adv. Space Res.* 68 (4) (2021) 1960–1974, <http://dx.doi.org/10.1016/j.asr.2021.04.032>.
- [30] G.S. Aglietti, B. Taylor, S. Fellowes, S. Ainley, D. Tye, C. Cox, A. Zarke, A. Mafficini, N. Vinkoff, K. Bashford, et al., RemoveDEBRIS: An in-orbit demonstration of technologies for the removal of space debris, *Aeronaut. J.* 124 (1271) (2020) 1–23, <http://dx.doi.org/10.1017/aer.2019.136>.
- [31] R. Axthelm, B. Klotz, I. Retat, U. Schlossstein, W. Tritsch, S. Vahsen, Net capture system for debris removal demonstration mission, in: *7th European Conference on Space Debris, ESOC, Darmstadt, Germany, 2017*.
- [32] E.M. Botta, Deployment and Capture Dynamics of Tether-Nets for Active Space Debris Removal (Ph.D. thesis), McGill University, Montreal, Québec, 2017.
- [33] B. Yost, S. Weston, State-of-the-art: Small spacecraft technology, *Small Spacecr. Syst. Virtual Inst. Natl. Aeronaut. Space Adm.* (2024).
- [34] D. Bourabah, C. Gnam, E.M. Botta, Inertia tensor estimation of tethered debris through tether tracking, *Acta Astronaut.* 212 (2023) 643–653, <http://dx.doi.org/10.1016/j.actaastro.2023.08.021>.
- [35] L. Field, D. Bourabah, E.M. Botta, Online estimation and control of tethered debris using tension and feature tracking, *J. Guid. Control Dyn.* 48 (2) (2025) 443–449, <http://dx.doi.org/10.2514/1.G008295>.
- [36] Y. Endo, H. Kojima, P.M. Trivailo, Study on acceptable offsets of ejected nets from debris center for successful capture of debris, *Adv. Space Res.* 66 (2) (2020) 450–461, <http://dx.doi.org/10.1016/j.asr.2020.04.012>.
- [37] M. Shan, J. Guo, E. Gill, Contact dynamics on net capturing of tumbling space debris, *J. Guid. Control Dyn.* 41 (9) (2018) 2063–2072, <http://dx.doi.org/10.2514/1.G003460>.
- [38] C. Zeng, G.R. Hecht, S. Chowdhury, E.M. Botta, Concurrent design optimization of tether-net system and actions for reliable space-debris capture, *J. Spacecr. Rockets* 1–11, <http://dx.doi.org/10.2514/1.A35812>.
- [39] A. Boonrath, E.M. Botta, Robustness and safety of net-based debris capture under deployment and environmental uncertainties, *J. Spacecr. Rockets* (2025) 1–17, <http://dx.doi.org/10.2514/1.A36217>.
- [40] Y. Zhao, F. Zhang, P. Huang, Capture dynamics and control of tethered space net robot for space debris capturing in unideal capture case, *J. Franklin Inst.* 357 (17) (2020) 12019–12036, <http://dx.doi.org/10.1016/j.jfranklin.2020.04.037>.
- [41] R. Biesbroek, T. Soares, J. Hüsing, K. Wormnes, L. Innocenti, The e. deorbit CDF study: a design study for the safe removal of a large space debris, in: *64th International Astronautical Congress, IAC, Beijing, 2013*.
- [42] W. Clohessy, R. Wiltshire, Terminal guidance system for satellite rendezvous, *J. Aerosp. Sci.* 27 (9) (1960) 653–658, <http://dx.doi.org/10.2514/8.8704>.
- [43] M. Shan, L. Shi, Analytical method for net deployment dynamics modeling and its experimental validation, *Acta Astronaut.* 200 (2022) 494–505, <http://dx.doi.org/10.1016/j.actaastro.2022.08.041>.
- [44] A. Boonrath, T. Singh, E.M. Botta, Identification of parameters for tethered satellite system to emulate net-captured debris towing, *Acta Astronaut.* (2024) <http://dx.doi.org/10.1016/j.actaastro.2024.09.022>.
- [45] M. Shan, J. Guo, E. Gill, W. Gołębowski, Validation of space net deployment modeling methods using parabolic flight experiment, *J. Guid. Control Dyn.* 40 (12) (2017) 3319–3327, <http://dx.doi.org/10.2514/1.G002761>.
- [46] H.D. Curtis, *Orbital mechanics for engineering students*, Revised fourth ed., Elsevier aerospace engineering series, Butterworth-Heinemann, An imprint of Elsevier, Kidlington, Oxford, United Kingdom, 2021.
- [47] E.M. Botta, I. Sharf, A.K. Misra, M. Teichmann, On the simulation of tether-nets for space debris capture with vortex dynamics, *Acta Astronaut.* 123 (2016) 91–102, <http://dx.doi.org/10.1016/j.actaastro.2016.02.012>.
- [48] SatCatalog, MR-106L 22N, 2024, [Online]. Available: <https://www.satcatalog.com/component/mr-106l-22n/>. (Last Accessed 29 April 2025).
- [49] J. Šílha, J.-N. Pittet, M. Hamara, T. Schildknecht, Apparent rotation properties of space debris extracted from photometric measurements, *Adv. Space Res.* 61 (3) (2018) 844–861, <http://dx.doi.org/10.1016/j.asr.2017.10.048>.
- [50] MatWeb, Teijin technora aramid fiber, 2024, [Online]. Available: <https://www.matweb.com/search/DataSheet.aspx?MatGUID=683f3be4a8e140a380b27cf05aa93229&ckck=1>. (Last Accessed 29 April 2025).
- [51] A. Ampatzoglou, V. Kostopoulos, Design, analysis, optimization, manufacturing, and testing of a 2U CubeSat, *Int. J. Aerosp. Eng.* 2018 (1) (2018) 972463, <http://dx.doi.org/10.1155/2018/972463>.
- [52] C. Nieto-Peroy, M.R. Emami, Cubesat mission: From design to operation, *Appl. Sci.* 9 (15) (2019) 3110, <http://dx.doi.org/10.3390/app9153110>.
- [53] SatCatalog, 2-unit CubeSat structure, 2017, [Online]. Available: <https://www.satcatalog.com/component/2-unit-cubesat-structure/>. (Last Accessed 29 April 2025).
- [54] Innovative Solutions in Space, Small satellite solar panels, 2024, [Online]. Available: <https://www.isispace.nl/product/isis-cubesat-solar-panels/>. (Last Accessed 29 April 2025).
- [55] GOM Space, NanoCam CIU, 2017, [Online]. Available: <https://gomspace.com/UserFiles/Subsystems/datasheet/gs-ds-nanocam-clu-17.pdf>. (Last Accessed 29 April 2025).
- [56] Innovative Solutions in Space, Compact electrical power system 2, 2024, [Online]. Available: <https://www.isispace.nl/product/compact-eps/>. (Last Accessed 29 April 2025).
- [57] Innovative Solutions in Space, ISIS on board computer, 2024, [Online]. Available: <https://www.isispace.nl/product/isospace-iobc/>. (Last Accessed 29 April 2025).
- [58] H. Hakima, M.R. Emami, Deorbiter CubeSat system engineering, *J. Astronaut. Sci.* 67 (4) (2020) 1600–1635, <http://dx.doi.org/10.1007/s40295-020-00220-5>.
- [59] Y.-K. Chen, Y.-C. Lai, W.-C. Lu, A. Lin, Design and implementation of high reliability electrical power system for 2U NutSat, *IEEE Trans. Aerosp. Electron. Syst.* 57 (1) (2020) 614–622, <http://dx.doi.org/10.1109/TAES.2020.3028488>.
- [60] S.S. Arnold, R. Nuzzaci, A. Gordon-Ross, Energy budgeting for CubeSats with an integrated FPGA, in: *2012 IEEE Aerospace Conference, IEEE, 2012*, pp. 1–14, <http://dx.doi.org/10.1109/AERO.2012.6187240>.



**Achira Boonrath** is an Aerospace Engineering Ph.D. candidate in the Department of Mechanical and Aerospace Engineering at the University at Buffalo (UB). Achira received his Bachelor of Science and Masters of Science in Aerospace Engineering from UB in 2022 and 2024, respectively. His primary research interest is in the simulation and modeling of flexible space systems designed for active debris removal.



**Federico Rossi** is a Robotics Technologist at the Jet Propulsion Laboratory, California Institute of Technology and the Planning, Scheduling, and Execution lead for NASA's CADRE lunar technology demonstration mission. He earned the Ph.D. degree in Aeronautics and Astronautics from Stanford University in 2018. His research focuses on distributed decision-making in multi-robot systems, with applications to planetary exploration and Earth science.



**Issa A.D. Nesnas** is a principal technologist at the Jet Propulsion Laboratory and associate director at Caltech's Center for Autonomous Systems and Technologies. He led research in architecting autonomous systems, in-space navigation for small bodies, surface navigation, tethered mobility for extreme terrains, and autonomous manipulation for space and industrial applications. For thirteen years, he served as the supervisor for the Robotic Mobility Group and the Robotic Software Group. He holds a B.E. degree in Electrical Engineering from Manhattan College, NY, and a M.S. and Ph.D. degrees in Mechanical Engineering from the University of Notre Dame, IN, in 1995. He is a member of NASA's Autonomous Systems Capability Leadership Team.



**Eleonora M. Botta** is an assistant professor in the Department of Mechanical and Aerospace Engineering at the University at Buffalo, NY. She received her Ph.D. in Mechanical Engineering from McGill University, QC, Canada in 2017, and holds degrees from Politecnico di Milano and Politecnico di Torino, Italy. Her main research interests are the dynamics and control of tethered space systems, spacecraft trajectory optimization, and space situational awareness. She is a senior member of AIAA and a member of AAS and IEEE. She is also the Chair of the AIAA Space Tethers Technical Committee, a member of the AAS Space Flight Mechanics Committee, and an Associate Editor for the AIAA Journal of Spacecraft and Rockets and for Advances in Space Research.